ARTICLES
https://doi.org/10.1038/s41563-021-00960-1

nature materials

Check for updates

Phonon renormalization in reconstructed MoS_2 moiré superlattices

Jiamin Quan[1,5], Lukas Linhart[1,2,5], Miao-Ling Lin[3], Daehun Lee[1], Jihang Zhu[1], Chun-Yuan Wang[1], Wei-Ting Hsu[1], Junho Choi[1], Jacob Embley[1], Carter Young[1], Takashi Taniguchi[4], Kenji Watanabe[4], Chih-Kang Shih[1], Keji Lai[1], Allan H. MacDonald[1], Ping-Heng Tan[3]✉, Florian Libisch[2]✉ and Xiaoqin Li[1]✉

In moiré crystals formed by stacking van der Waals materials, surprisingly diverse correlated electronic phases and optical properties can be realized by a subtle change in the twist angle. Here, we discover that phonon spectra are also renormalized in MoS_2 twisted bilayers, adding an insight to moiré physics. Over a range of small twist angles, the phonon spectra evolve rapidly owing to ultra-strong coupling between different phonon modes and atomic reconstructions of the moiré pattern. We develop a low-energy continuum model for phonons that overcomes the outstanding challenge of calculating the properties of large moiré supercells and successfully captures the essential experimental observations. Remarkably, simple optical spectroscopy experiments can provide information on strain and lattice distortions in moiré crystals with nanometre-size supercells. The model promotes a comprehensive and unified understanding of the structural, optical and electronic properties of moiré superlattices.

In vertical van der Waals homo- or heterobilayers with weak interlayer coupling, a finite twist angle between layers leads to a moiré superlattice that induces periodic modulations of atomic structure, energy and optical selection rules[1,2]. Controlling the twist angle with ~0.05–0.1° accuracy[3] in graphene bilayers near the magic angles leads to completely different correlated electronic phases including superconductivity[4,5], orbital magnetism[6,7] and correlated insulator states[8]. Similar phenomena have been observed in transition metal dichalcogenide (TMD) twisted bilayers (TBLs)[9–11], although with a reduced sensitivity to the twist angle[12,13]. In WSe_2 TBLs, correlated insulating states are observed over a broad range of twist angles between 4° and 5.1°, indicating intriguing changes over a magic twist angle continuum[13].

Those prior experiments on moiré superlattices have been interpreted using a rigid lattice model in which the local atomic stacking is assumed to be determined by rotating pristine two-dimensional (2D) lattices. However, theoretical studies and microscopy experiments have shown that substantial lattice relaxation can occur in TMD TBLs[14–18]. Recent piezoresponse force microscopy (PFM) and scanning transmission electron microscopy (STEM)[17,18] measurements reveal a tessellated pattern of mirror-reflected triangular domains in TMD TBLs, separated by a network of thin domain boundaries for twist angles $\theta < 2°$. This precise structural information challenges the interpretations of previous experiments based on a rigid lattice picture.

In this work, we reveal an intricate connection between phonon spectra and moiré lattice reconstruction. Our discoveries are enabled by Raman measurements on a series of MoS_2 TBLs with precisely controlled twist angles and by a theoretical approach for calculating moiré phonons. With increasing twist angle, reconstructed moiré lattices can be categorized into three different regimes. In the relaxed ($0° \leq \theta < 2°$) and rigid ($\theta \geq 6°$) regimes, the Raman spectra hardly change with the twist angle. In the transition regime ($2° \leq \theta < 6°$), however, low-frequency interlayer shear (S) and layer breathing (LB) modes evolve rapidly with twist angle. This evolution is driven by lattice reconstruction and ultra-strong coupling of different phonon modes. We further attribute a splitting of the commonly observed high-frequency intralayer E_{2g} mode to the local distortion of the hexagonal lattice within each monolayer. The excellent agreement between experiment and theory allows us to unambiguously identify phonon hybridization in the 'magic continuum' angle range. In the big picture, we thus open an important 'phonon' perspective on recently observed strong correlation physics in TMDs. By measuring and analysing moiré-scale wavelength phonons, we show that these degrees of freedom have their own unique moiré physics.

Atomic reconstruction in twisted bilayers

The atomic reconstruction of the moiré pattern is determined by a twist-angle-dependent competition between strain and interlayer coupling[15,17,19–21], as shown in Fig. 1 (Supplementary Discussion I for detailed calculation). At small twist angles, the real space supercell is very large, allowing substantial lattice relaxation even though it is driven by weak van der Waals interactions between the layers and inhibited by strong in-plane bonding within each layer. The relaxation pattern forms large triangular regions in which the energetically favourable stacking configurations (Fig. 1c right column and Supplementary Discussion I) known as AB(BA) stacking (or 3R stacking for $\theta = 0°$; Supplementary Discussion II) are approached[15,22]. The local strain (left column in Fig. 1c) in the relaxed regime peaks along domain boundaries and at topological defects[23] with AA stacking where domains intersect.

As the twist angle increases and real space supercell size decreases, the distance between neighbouring AB and BA stacking

[1]Department of Physics, The University of Texas at Austin, Austin, TX, USA. [2]Institute for Theoretical Physics, Vienna University of Technology, Vienna, Austria. [3]State Key Laboratory of Superlattices and Microstructures, Institute of Semiconductors, Chinese Academy of Sciences, Beijing, China. [4]National Institute for Material Science, Tsukuba, Japan. [5]These authors contributed equally to this work: Jiamin Quan, Lukas Linhart. ✉e-mail: phtan@semi.ac.cn; florian.libisch@tuwien.ac.at; elaineli@physics.utexas.edu

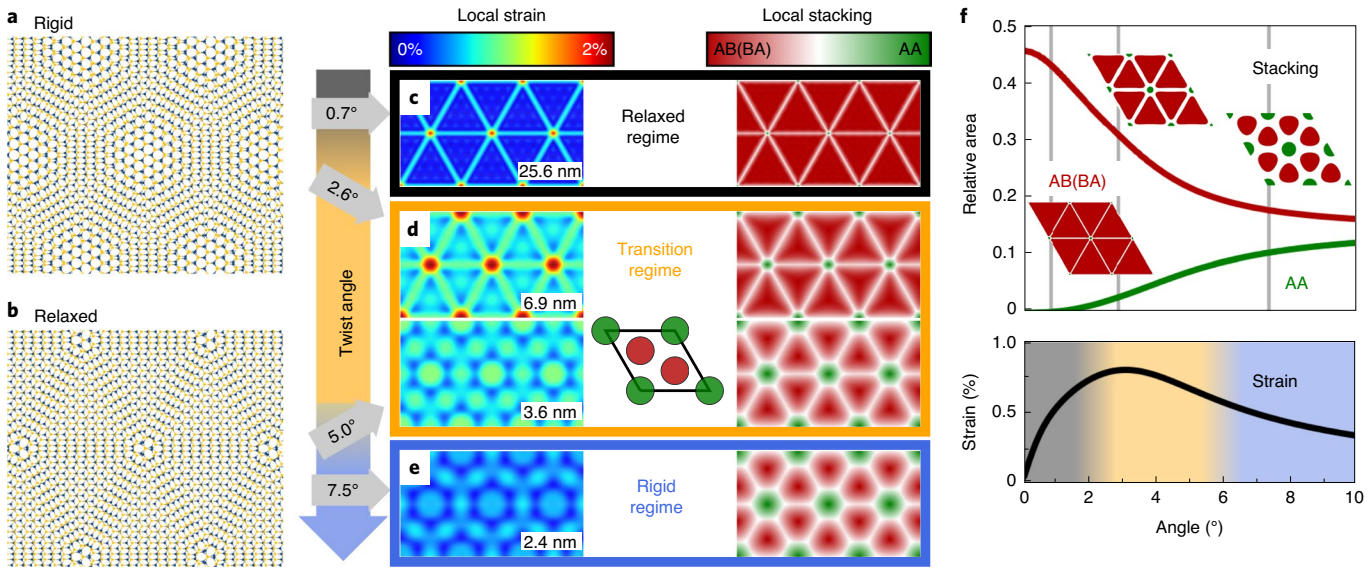

Fig. 1 | Twist-angle-dependent lattice reconstruction in MoS_2 TBLs with small twist angles. a,**b**, Two rotated layers of MoS_2 without (**a**) and with (**b**) lattice relaxation (exaggerated for clarity). **c**–**e**, Calculated patterns of local strain (left column) and stacking (right column) at various twist angles. The plots are drawn in moiré cell units to facilitate comparison of quasi-periodic supercells of different sizes. Three distinct lattice reconstruction regimes can be identified: the relaxed regime (black rectangle, **c**), the transition regime (orange rectangle, **d**) and the rigid regime (blue rectangle, **e**). The inset illustrates the area of AA (dark green) and AB(BA) (dark red) stacking within a rigidly rotated bilayer. **f**, The top shows the fraction of the total area covered by AB(BA) (dark red) or AA (dark green) stacking. Area is counted as AA/AB(BA) if the relative displacement between the layers is smaller than 0.25 times the lattice constant. The insets represent three representative lattice stackings corresponding to twist angles at 0.7°, 2.6° and 7.5° (grey lines). The bottom shows the evolution of the average (local) strain in the system (exact definition as in Supplementary Discussion I).

configurations is reduced (Fig. 1d). Correspondingly, the area occupied by the domain walls that interpolate between them increases steadily across a transition regime. Finally, the TBL reaches the rigid regime at large twist angles ($\theta \geq 6°$). In this regime (Fig. 1e), the area with nearly perfect low-energy and high-symmetry AB(BA) stacking is small. The resulting reduction of strain leads to essentially flat[24] rigid layers[15,25]. The evolution of the low-energy AB(BA) area (red line) and the high-energy AA area (green line) as a function of twist angle is summarized in Fig. 1f (top), while the area-averaged strain is summarized in Fig. 1f (bottom). These variations of atomic configuration and local strain are expected to modulate the lattice vibrations.

Strain and coupled phonons observed by Raman spectroscopy

We measured Raman spectra from a series of MoS_2 TBLs with accurately controlled twist angles in the range $0° \leq \theta \leq 20°$. Details of the sample preparation procedure and Raman measurements are discussed in the Methods and Supplementary Discussion III. The measured spectra feature several phonon modes divided into the low-frequency (Fig. 2a) and high-frequency ranges (Fig. 2b). The low-frequency Raman spectra exhibit two types of phonon modes, the interlayer S and LB modes, in which the relative motion of the two monolayers is parallel or perpendicular to the 2D layers, respectively[26–29] (Fig. 2a top). These two types of phonon modes are identified based on their distinct polarization dependence in polarization-resolved Raman measurements. The LB Raman modes have a fine structure due to coupling to discrete LB modes of the hexagonal boron nitride (hBN) substrate with a finite thickness[30] (Supplementary Discussion V). We remove this fine structure[30] (Supplementary Fig. 6) to focus on the main features related to moiré pattern reconstruction via a fast Fourier transform filter (Supplementary Discussions VI and VII). As the twist angle increases, one branch of the LB mode (LB_1) blueshifts and seems to disappear along with the S mode, while a second branch of the LB mode (LB_2) emerges. In the high-frequency Raman spectra there are two dominant intralayer modes (Fig. 2b), commonly denoted as E_{2g} (385 cm^{-1}) and A_{1g} (407 cm^{-1}) following the assignments appropriate for the D_{6h} symmetry of bulk (2H stacked) MoS_2 (refs. [31,32]). The two-fold degenerate E_{2g} mode originates from opposite motions of two sulfur atoms relative to the Mo atom within the 2D plane, while the A_{1g} mode arises from the out-of-plane relative vibrations of the sulfur atoms[31,33] (Fig. 2b top). Although the A_{1g} mode frequency is nearly independent of twist angle, the E_{2g} mode evolves into a doublet in the $2° \leq \theta < 6°$ transition regime, which we will discuss in more detail below. While Raman measurement on TMD TBLs has previously been reported[24,34–37], those experiments were performed on samples with much less control of twist angle and missed the systematic phonon renormalization captured by our experiments.

The evolution of the Raman spectra is further analysed by tracking the peak positions and linewidths as a function of twist angle (Fig. 3a–c). Distinct features emerge in the three regimes. In the relaxed regime ($0° \leq \theta < 2°$), the frequencies and linewidths of all modes exhibit little change because the moiré patterns remain qualitatively the same (matching the $\theta = 0°$ case[26]) with only quantitative changes in the AB(BA) domain area. In the transition regime ($2° \leq \theta < 6°$), the phonon spectra change drastically. The S mode broadens and quickly disappears. There is also a rapid and systematic change in the frequency and intensity (Supplementary Discussion IX). Prominently, the evolution of the LB modes resembles an anticrossing behaviour (Fig. 3a) typically observed when hybrid modes form due to coupling between different phonon modes, as we explain below. The linewidth of each phonon mode directly reflects the phonon lifetime. Assuming[38] that the linewidth γ is related to the lifetime τ by $\tau = \hbar/\gamma$, where $\hbar$ is the reduced Planck's constant, we find that the lifetime of the LB_1 mode is 49 ps and 7.1 ps for TBLs at 2° and 3.3°, respectively. These drastic changes in phonon frequency and lifetime in the transition regime may be

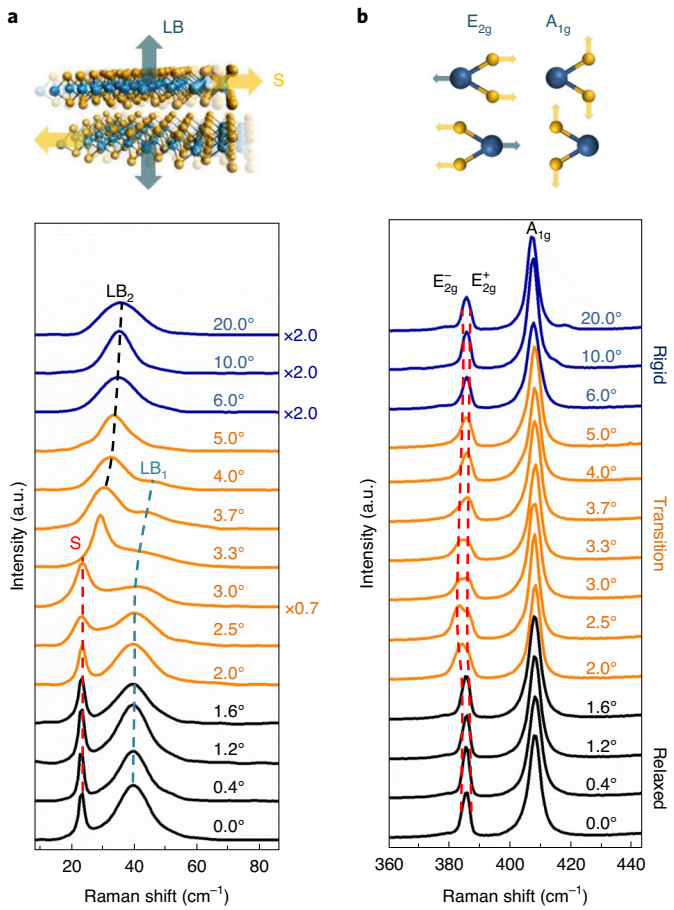

Fig. 2 | Measured Raman spectra of MoS_2 TBLs as a function of twist angle. **a**, Interlayer phonon modes including the S mode and two LB modes (LB_1 and LB_2). **b**, Intralayer phonon modes and the measured Raman spectra including the two E^+_{2g} (E^-_{2g}) modes and one A_{1g} mode. The spectra are scaled and offset for clarity and the scale factors are shown on the edge of the panel; note that scale factors of 1.0 are omitted. The illustrations at the top show the schematic diagrams of the atomic eigenvectors for each phonon mode. The S mode (LB modes) corresponds to in-plane (out-of-plane) relative motions of the constituent layers; the E_{2g} mode corresponds to in-plane relative motion between molybdenum and sulfur atoms; and the A_{1g} mode corresponds to out-of-plane sulfur atom vibrations.

used to infer twist angle and supercell size on the basis of the TBL Raman spectra alone, offering a simple and powerful spectroscopy technique to characterize moiré crystals. The onset of the transition regime identified by Raman spectra at θ of ~2° agrees remarkably well with a very recent STEM study performed on mechanically stacked MoS_2 TBLs[17]. Finally, in the rigid regime with $\theta \geq 6°$, incommensurate stacking again results in stable Raman spectra with little dependence on the twist angle. In this regime, the exponential dependence of the polarizability on the layer separation substantially reduces the intensity of the S mode, explaining why it is not observed in our experiments[24,34,35] (Supplementary Discussion X).

Clear signatures of three reconstruction regimes are also found in the high-frequency E_{2g} mode (Fig. 3c). In the relaxed regime, strain is absent except on the sharp domain walls. Since domain walls only account for a small fraction of the total sample area in the relaxed regime, their influence is not observed in our far-field measurements but may be revealed in near-field measurements[14]. Meanwhile, strain is too small in the rigid regime. Thus, no clear peak splitting is observed in either of these two regimes. By contrast, the mode splits into a doublet E^+_{2g} and E^-_{2g} in the transition regime due to local strain caused by the atomic reconstruction. High strain locally distorts the hexagonal unit cell and breaks the three-fold rotational symmetry, ultimately causing the E_{2g} mode to split[39,40] (Fig. 3d). Based on a two-peak fitting (Supplementary Discussion VI), the largest splitting of the E_{2g} mode, up to 3.2 cm^{-1}, occurs at the $\theta = 2.5°$ TBL, where the influence of strain on hexagonal symmetry is maximal (Fig. 1f bottom). Notably, our measurements report averaged strain under the laser spot. Local variations of strain within a moiré supercell can be resolved using a near-field technique[14]. However, reaching a sufficient spatial resolution in the transition regime, where the supercell size ranges from 9 nm (2°) to 3 nm (6°), would be very challenging. Previous Raman spectroscopy experiments on TBLs[24,35,41–46] with less accurate twist angle control have focused on the electronic enhancement of the Raman signal or on moiré folded phonons. They have been explained via pristine cell calculations[26], simple zone folding[41] and effective force constant models[30]. While twist-angle-dependent phonon modes have been predicted in supercell calculations[42,47], their relation to lattice reconstruction and mode hybridization[48] has not been observed experimentally.

We confirm the presence of atomic reconstructions in a TBL at a θ of ~0.08° by PFM measurements. The large strain gradients near the AA stacking regions and the domain walls (Fig. 1c–e) allow piezoelectric coupling to an out-of-plane a.c. electric field[18] (Methods). PFM data in Fig. 3e clearly reveal the reconstructed moiré superlattice with a typical size of ~230 nm as expected. The superlattice is divided into large triangular AB/BA domains by narrow domain walls that locally break the single-layer D_{3h} symmetry (Fig. 3d). The results confirm the high quality of our samples and the expected moiré reconstructions in the relaxed regime.

A continuum model to understand phonon renormalization

Simple models such as phonon dispersion folding[41] or force constant models[27,30,42] previously developed to describe Raman experiments in bilayers cannot explain the complicated evolution of modes we observe. Full ab initio calculations become too expensive at small twist angles[24] and are, like effective force constant models of supercells[47], limited to commensurate twist angles (Fig. 4a). Here, we adapt a low-energy continuum model approach, developed by Bistritzer and MacDonald[49,50], to calculate the electronic system of moiré superlattices, to phonons in TBLs (Supplementary Discussion XI for details). The pristine lattice vectors $\mathbf{a}_1 = (a_0, 0)$, $\mathbf{a}_2 = a_0(-1, \sqrt{3})/2$ (Fig. 4b) define the adjoint reciprocal lattice vectors $\mathbf{G}$. In the small angle limit, the relationship between the displacement $\mathbf{d}$ between layers (which characterizes local stacking) and position within the moiré pattern maps $\mathbf{G}$ onto the reciprocal lattice vectors $\tilde{\mathbf{G}}$ of the moiré cell via $\tilde{\mathbf{G}}(\theta, \mathbf{G}) \approx -\theta\hat{z} \times \mathbf{G}$ (Fig. 4c), with $\hat{z}$ the out-of-plane unit vector. We calculate phonon modes from local crystalline dynamical matrices $\bar{D}$ evaluated as a function of the displacement $\mathbf{d}$ (Fig. 4b). To calculate the optically active phonon modes near the central $\mathbf{\Gamma}$ point, we assemble the moiré dynamical matrix $\bar{D}_m(\mathbf{q}, \mathbf{q}')$ from matrices $\bar{D}(\mathbf{q}|\mathbf{d})$ evaluated for each local stacking $\mathbf{d}$ via Fourier transform,

$$\bar{D}_m(\mathbf{q}, \mathbf{q}') = \sum_{\mathbf{G},\mathbf{d}} \delta\left(\mathbf{q} - \mathbf{q}' - \tilde{\mathbf{G}}(\theta, \mathbf{G})\right) \bar{D}(\mathbf{q}'|\mathbf{d}) e^{i\mathbf{d}\cdot\mathbf{G}}. \quad (1)$$

This moiré dynamical matrix is off-diagonal in the reciprocal space variable $\mathbf{q}^{(\prime)}$ because of the slow spatial variation of $\mathbf{d}$. We find that small $|\mathbf{G}|$ terms dominate in equation (1), allowing us to truncate the sum after the first shell of six non-zero reciprocal lattice vectors, coupling each $\mathbf{q}$ point in the moiré reciprocal unit cell to six replicas. In particular, the central $\mathbf{\Gamma}$ point is coupled to six neighbours $\tilde{\mathbf{G}}_{1\ldots6}$ (blue dots in Fig. 4c). The $\bar{D}(\mathbf{q}|\mathbf{d})$ for each displacement $\mathbf{d}$ can be straightforwardly obtained from density functional perturbation theory. This model does not include any free parameters.

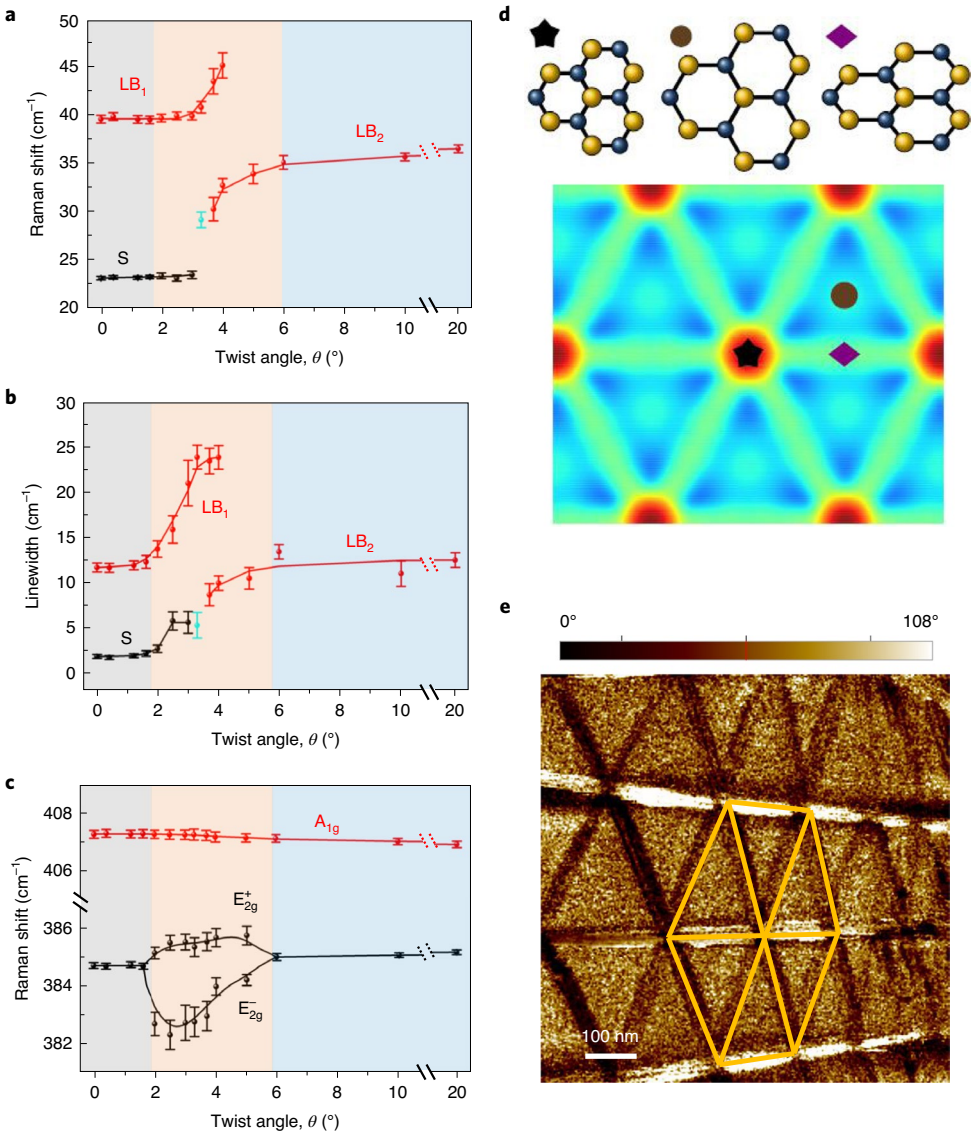

Fig. 3 | Analysis of the Raman spectra and experimentally observed lattice reconstruction. a,**b**, Central frequencies (**a**) and linewidths (**b**) of S, LB_1 and LB_2 as a function of the twist angle. The cyan dots in **a** and **b** refer to a mode that cannot be uniquely identified as LB or S. **c**, The central frequencies of intralayer modes as a function of twist angle. The error bars in **a**–**c** represent the uncertainty of the fitting parameter in the fitting process (Supplementary Discussion VI). **d**, Pictorial illustration of local strain at various positions within the moiré pattern: compressive at the AA (black star) stacking, tensile at AB (brown circle) stacking and uniaxial along the domain boundaries (violet diamond). The corresponding positions are indicated in the strain pattern of Fig. 1d. **e**, PFM phase image of reconstructed moiré superlattices at $\theta \approx 0.08°$.

When truncating the expansion after the first shell, our model yields a total of 126 modes, that is, 18 modes that are folded by the moiré reciprocal lattice and evolve continuously with twist angle. Mode energies calculated at the $\mathbf{\Gamma}$ point of MoS_2 probed by Raman spectroscopy, neglecting or including lattice relaxation, are shown in Fig. 4d or 4e, respectively. We rescale the overall interlayer coupling strength by a single factor of 1.15 to match the interlayer frequencies at $\theta = 0°$ to the experiment (Supplementary Discussion XI).

The LB modes are only weakly twist-angle dependent in both the relaxed ($LB_1 \approx 40\,cm^{-1}$) and the rigid ($LB_2 \approx 33\,cm^{-1}$) regimes (Fig. 4e). Calculations and measurements match perfectly for the LB modes at all θ. We find a prominent anticrossing of the LB modes caused by coupling to the dispersive folded transverse acoustic modes, in excellent agreement with the experimental evolution of the LB modes in the transition regime (Fig. 3a). At $\theta \approx 3.5°$, the folded transverse acoustic phonon modes originating at $\tilde{\mathbf{G}} = \tilde{\mathbf{G}}_1 \ldots \tilde{\mathbf{G}}_6$ (grey lines in Fig. 4d) are degenerate with the LB mode at $\mathbf{q} = \mathbf{\Gamma}$. The ultra-strong coupling between the two modes can be explained by the large $\mathbf{d}$ dependence of $\bar{D}(\mathbf{q}'|\mathbf{d})$ in the corresponding spacial direction. By comparing calculations without (Fig. 4d) and with (Fig. 4e) lattice relaxations, one recognizes that the LB modes are similar in both cases. Thus, although the rapid evolution of the LB modes coincides with the transition regime, our calculations suggest that this is not caused by the atomic reconstructions of the moiré pattern.

Only when accounting for relaxation of the lattice via elasticity theory (Fig. 4e and Supplementary Discussions I and XI (section C)), the instability (for example, imaginary frequency for the S mode) of the rigid TBLs for $\theta \lesssim 4°$ is removed. At small twist angles, lattice reconstruction causes the degenerate S mode frequencies to shift and match the measured values. For larger angles, our model overestimates the corrugation (variation of layer separation in **d**)

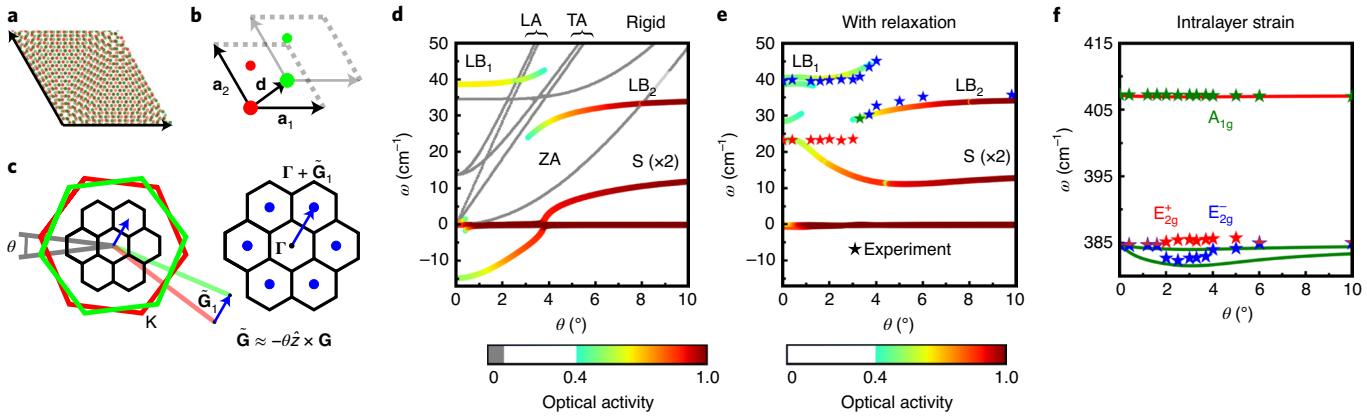

Fig. 4 | Calculated evolution of phonon modes as a function of twist angle θ. **a**, Real space representation of MoS_2 TBL at $\theta = 3.9°$. Atoms of the top (bottom) layer are illustrated in green (red). **b**, Locally stacked pristine unit cells. **c**, Reciprocal representation of the moiré Brillouin zone (central black hexagons) and its relation to the pristine Brillouin zones (green and red). Blue arrows indicate relation to neighbouring moiré $\mathbf{\Gamma}$ points. **d**,**e**, Low-energy phonon evolution at $\mathbf{q} = \mathbf{\Gamma}$, neglecting (**d**) or including (**e**) lattice relaxation as a function of twist angle θ. The deviations of the S mode at intermediate twist angles are discussed in detail in Supplementary Discussion X. Colour codes are based on optical activity (colour bar) as approximated by projecting the phonon eigenmodes $\mathbf{Q}_i$ onto the central $\mathbf{\Gamma}$ point, $|\langle \mathbf{Q}_i | \mathbf{\Gamma} \rangle|^2$. Grey lines in **d** show optically inactive modes entirely originating at neighbouring moiré $\mathbf{\Gamma}$ points (blue dots in **c**). TA, transverse acoustic; LA, longitudinal acoustic; ZA, out-of-plane acoustic; ×2 indicates the degeneracy of the S mode. **f**, Twist-angle-dependent evolution of the optical phonon modes A_{1g} (red line) and the degeneracy lifted $E^{\pm}_{2g}$ modes (green line). Stars in **e** and **f** indicate the corresponding experimental values. Calculated optical mode energies are shifted to match the experimental values at $\theta = 0°$.

of the moiré pattern[24], causing deviations between the calculated and measured S mode frequencies (Supplementary Discussion X). Neglecting its atomistic structure, the moiré patterns preserve C_3 symmetry even in the presence of lattice relaxation and therefore conserve the degeneracy of the S mode at the $\mathbf{\Gamma}$ point present for $\theta = 0°$. Given the complex interplay of layer separation, mode coupling and lattice reconstruction, a detailed explanation for the behaviour of the linewidth is outside the scope of the present work.

We also calculate the evolution of the A_{1g} and E_{2g} Raman peaks with twist angle. While the optically active A_{1g} mode is hardly affected by the moiré, local strain lifts the degeneracy of the E_{2g} mode by breaking the hexagonal symmetry[39,40]. The non-uniform strain present in moiré structures (Fig. 1c–e) becomes uniaxial at the domain walls (Fig. 3d), breaking the single-layer D_{3h} symmetry and causing splitting of the E_{2g} mode into $E^{\pm}_{2g}$ (ref. [39]). The observed proportionality between the splitting $E^{+}_{2g} - E^{-}_{2g}$ (Fig. 4f) and the average strain (Fig. 1f) further corroborates our model and underpins the crucial role of strain in these systems.

Summary and outlook

In summary, our study reveals that phonon spectra are renormalized in reconstructed MoS_2 moiré superlattices. We discover three regimes of atomic reconstructions characterized by distinct Raman spectra. We anticipate that these regimes and the phonon renormalization will occur in other TBLs although the range of the twist angle could vary. The most interesting Raman spectral changes in the transition regime suggest a continuous and subtle evolution of atomic configurations and strain. Such information is partially accessible via scanning tunnelling microscopy[14] but challenging for many common scanning probe and near-field techniques. In the same regime, a rich variety of electronic phases in TMD TBLs have been reported[13], highlighting the importance of reconciling electronic phases with static and dynamic lattice properties. To treat the phononic and electronic degrees of freedom on an equal footing, we introduce a computationally efficient method to describe phonons in moiré crystals at any small twist angle, which can be extended to describe electron–phonon interaction in the future. Thus, our work is also a necessary step towards addressing the influence of electron–phonon interactions on the Wigner crystal state stability[9], magnetic order[10] and metal–insulator transitions[13] in TMD moiré materials.

Online content

Any methods, additional references, Nature Research reporting summaries, source data, extended data, supplementary information, acknowledgements, peer review information; details of author contributions and competing interests; and statements of data and code availability are available at https://doi.org/10.1038/s41563-021-00960-1.

Received: 12 May 2020; Accepted: 16 February 2021;
Published online: 22 March 2021

References

1. Zhang, C. et al. Interlayer couplings, moiré patterns, and 2D electronic superlattices in MoS_2/WSe_2 hetero-bilayers. *Sci. Adv.* **3**, e1601459 (2017).
2. Tran, K. et al. Evidence for moiré excitons in van der Waals heterostructures. *Nature* **567**, 71–75 (2019).
3. Kim, K. et al. van der Waals heterostructures with high accuracy rotational alignment. *Nano Lett.* **16**, 1989–1995 (2016).
4. Cao, Y. et al. Unconventional superconductivity in magic-angle graphene superlattices. *Nature* **556**, 43–50 (2018).
5. Yankowitz, M. et al. Tuning superconductivity in twisted bilayer graphene. *Science* **363**, 1059–1064 (2019).
6. Sharpe, A. L. et al. Emergent ferromagnetism near three-quarters filling in twisted bilayer graphene. *Science* **365**, 605–608 (2019).
7. Serlin, M. et al. Intrinsic quantized anomalous hall effect in a moiré heterostructure. *Science* **367**, 900–903 (2020).
8. Cao, Y. et al. Correlated insulator behaviour at half-filling in magic-angle graphene superlattices. *Nature* **556**, 80–84 (2018).
9. Regan, E. C. et al. Mott and generalized Wigner crystal states in WSe_2/WS_2 moiré superlattices. *Nature* **579**, 359–363 (2020).
10. Tang, Y. et al. Simulation of Hubbard model physics in WSe_2/WS_2 moiré superlattices. *Nature* **579**, 353–358 (2020).
11. Shimazaki, Y. et al. Strongly correlated electrons and hybrid excitons in a moiré heterostructure. *Nature* **580**, 472–477 (2020).
12. Naik, M. H. & Jain, M. Ultraflatbands and shear solitons in moiré patterns of twisted bilayer transition metal dichalcogenides. *Phys. Rev. Lett.* **121**, 266401 (2018).
13. Wang, L. et al. Correlated electronic phases in twisted bilayer transition metal dichalcogenides. *Nat. Mater.* **19**, 861–866 (2020).
14. Gadelha, A. C. et al. Localization of lattice dynamics in low-angle twisted bilayer graphene. *Nature* **590**, 405–409 (2021).

15. Carr, S. et al. Relaxation and domain formation in incommensurate two-dimensional heterostructures. *Phys. Rev. B* **98**, 224102 (2018).
16. Sushko, A. et al. High resolution imaging of reconstructed domains and moiré patterns in functional van der Waals heterostructure devices. Preprint at https://arXiv.org/abs/1912.07446 (2019).
17. Weston, A. et al. Atomic reconstruction in twisted bilayers of transition metal dichalcogenides. *Nat. Nanotechnol.* **15**, 592–597 (2020).
18. McGilly, L. J. et al. Visualization of moiré superlattices. *Nat. Nanotechnol.* **15**, 580–584 (2020).
19. Jung, J., DaSilva, A. M., MacDonald, A. H. & Adam, S. Origin of band gaps in graphene on hexagonal boron nitride. *Nat. Commun.* **6**, 6308 (2015).
20. Rosenberger, M. R. et al. Twist angle-dependent atomic reconstruction and moiré patterns in transition metal dichalcogenide heterostructures. *ACS Nano* **14**, 4550–4558 (2020).
21. Yoo, H. et al. Atomic and electronic reconstruction at the van der Waals interface in twisted bilayer graphene. *Nat. Mater.* **18**, 448–453 (2019).
22. Zhang, K. & Tadmor, E. B. Structural and electron diffraction scaling of twisted graphene bilayers. *J. Mech. Phys. Solids* **112**, 225–238 (2018).
23. Alden, J. S. et al. Strain solitons and topological defects in bilayer graphene. *Proc. Natl Acad. Sci. USA* **110**, 11256–11260 (2013).
24. Huang, S. et al. Low-frequency interlayer Raman modes to probe interface of twisted bilayer MoS_2. *Nano Lett.* **16**, 1435–1444 (2016).
25. Nam, N. N. & Koshino, M. Lattice relaxation and energy band modulation in twisted bilayer graphene. *Phys. Rev. B* **96**, 075311 (2017).
26. Molina-Sánchez, A. & Wirtz, L. Phonons in single-layer and few-layer MoS_2 and WS_2. *Phys. Rev. B* **84**, 155413 (2011).
27. Tan, P. et al. The shear mode of multilayer graphene. *Nat. Mater.* **11**, 294–300 (2012).
28. Zhang, X. et al. Raman spectroscopy of shear and layer breathing modes in multilayer MoS_2. *Phys. Rev. B* **87**, 115413 (2013).
29. Zhao, Y. et al. Interlayer breathing and shear modes in few-trilayer MoS_2 and WSe_2. *Nano Lett.* **13**, 1007–1015 (2013).
30. Lin, M.-L. et al. Cross-dimensional electron-phonon coupling in van der Waals heterostructures. *Nat. Commun.* **10**, 2419 (2019).
31. Lee, C. et al. Anomalous lattice vibrations of single- and few-layer MoS_2. *ACS Nano* **4**, 2695–2700 (2010).
32. Verble, J. L. & Wieting, T. J. Lattice mode degeneracy in MoS_2 and other layer compounds. *Phys. Rev. Lett.* **25**, 362–364 (1970).
33. Li, H. et al. From bulk to monolayer MoS_2: evolution of Raman scattering. *Adv. Funct. Mater.* **22**, 1385–1390 (2012).
34. Puretzky, A. A. et al. Twisted $MoSe_2$ bilayers with variable local stacking and interlayer coupling revealed by low-frequency Raman spectroscopy. *ACS Nano* **10**, 2736–2744 (2016).
35. Holler, J. et al. Low-frequency Raman scattering in WSe_2–$MoSe_2$ heterobilayers: evidence for atomic reconstruction. *Appl. Phys. Lett.* **117**, 013104 (2020).
36. Liao, M. et al. Precise control of the interlayer twist angle in large scale MoS_2 homostructures. *Nat. Commun.* **11**, 2153 (2020).
37. Debnath, R. et al. Evolution of high-frequency Raman modes and their doping dependence in twisted bilayer MoS_2. *Nanoscale* **12**, 17272–17280 (2020).
38. Cuscó, R., Gil, B., Cassabois, G. & Artús, L. Temperature dependence of Raman-active phonons and anharmonic interactions in layered hexagonal BN. *Phys. Rev. B* **94**, 155435 (2016).
39. Lee, J.-U. et al. Strain-shear coupling in bilayer MoS_2. *Nat. Commun.* **8**, 1370 (2017).
40. Wang, Y., Cong, C., Qiu, C. & Yu, T. Raman spectroscopy study of lattice vibration and crystallographic orientation of monolayer MoS_2 under uniaxial strain. *Small* **9**, 2857–2861 (2013).
41. Lin, M.-L. et al. Moiré phonons in twisted bilayer MoS_2. *ACS Nano* **12**, 8770–8780 (2018).
42. Koshino, M. & Son, Y.-W. Moiré phonons in twisted bilayer graphene. *Phys. Rev. B* **100**, 075416 (2019).
43. Campos-Delgado, J., Cançado, L. G., Achete, C. A., Jorio, A. & Raskin, J.-P. Raman scattering study of the phonon dispersion in twisted bilayer graphene. *Nano Res.* **6**, 269–274 (2013).
44. He, R. et al. Observation of low energy Raman modes in twisted bilayer graphene. *Nano Lett.* **13**, 3594–3601 (2013).
45. Cocemasov, A. I., Nika, D. L. & Balandin, A. A. Phonons in twisted bilayer graphene. *Phys. Rev. B* **88**, 035428 (2013).
46. Jorio, A. & Cançado, L. G. Raman spectroscopy of twisted bilayer graphene. *Solid State Commun.* **175**, 3–12 (2013).
47. Maity, I., Naik, M. H., Maiti, P. K., Krishnamurthy, H. & Jain, M. Phonons in twisted transition-metal dichalcogenide bilayers: ultrasoft phasons and a transition from a superlubric to a pinned phase. *Phys. Rev. Res.* **2**, 013335 (2020).
48. Cocemasov, A. I., Nika, D. L. & Balandin, A. A. Phonons in twisted bilayer graphene. *Phys. Rev. B* **88**, 035428 (2013).
49. Jung, J., Raoux, A., Qiao, Z. & MacDonald, A. H. *Ab initio* theory of moiré superlattice bands in layered two-dimensional materials. *Phys. Rev. B* **89**, 205414 (2014).
50. Bistritzer, R. & MacDonald, A. H. Moiré bands in twisted double-layer graphene. *Proc. Natl Acad. Sci. USA* **108**, 12233–12237 (2011).

Methods

Sample preparation. The samples were fabricated using a modified tear-and-stack technique[3]. A schematic diagram of the stacking process is presented in Supplementary Fig. 3a. The hBN and monolayer MoS_2 flakes were mechanically exfoliated from a bulk crystal onto a polydimethylsiloxane sheet. The hBN thickness was typically around 15 nm, measured by atomic force microscopy. The MoS_2 monolayer was identified by optical contrast spectroscopy and Raman spectroscopy. The bottom hBN was first transferred onto the Si/SiO_2 (90 nm) substrate and subsequently annealed at 500 °C for 10 h. The van der Waals force between hBN and the MoS_2 monolayer was used to tear a part off the monolayer flake at room temperature, which was transferred onto the hBN. The separated monolayer pieces were rotated by a specific angle and stacked together. The accuracy in controlling the twist angle was ~0.1°. Finally, the samples were annealed under ultrahigh vacuum (around 10^{-5} mbar) to enhance the coupling between two layers. To avoid possible rotations between the layers, a relatively low temperature (150 °C) and a short process time (2 h) was used for the annealing. We carefully checked the microscope images before and after annealing and found no rotations during the annealing for all samples (Supplementary Fig. 3b,c). The spatial uniformity of the optical properties of the TBLs was futher confirmed via low-frequency Raman mapping (Supplementary Fig. 4).

Raman measurement. Raman spectra were measured at room temperature using a Princeton Acton 7500i spectrometer equipped with a liquid-nitrogen-cooled charge-coupled detector, with a ×100 objective lens (numerical aperture, 0.90). BragGrate notch filters were used to reject the Rayleigh scattering down to 8 cm^{-1}. The excitation laser was a 532 nm (that is, 2.33 eV) continuous-wave laser from a Verdi V10. A grating with 1,200 lines mm^{-1} was used in the Raman measurements. An incident laser power of 0.2 mW was used to avoid sample heating. The excitation laser and collected Raman signal were collinearly polarized.

PFM measurements. In a PFM measurement, an a.c. bias is applied on the conductive tip to induce sample deformation through the piezoelectric effect. The amplitude and phase of vertical (out-of-plane) and horizontal (in-plane) deformations of the sample are recorded during the contact-mode scan, providing local information of the electromechanical response. The experiments were performed on a commercial atomic force microscope (XE-70 AFM, Park Systems). A lock-in amplifier (HF2LI, Zurich Instruments) was used to apply the a.c. bias (typically around 1 V) and demodulate the PFM signals. The radius of the cantilever probe (ANSCM-PT-10, App Nano) was less than 30 nm, and the force constant was ~1–5 N m^{-1}. For out-of-plane PFM, the first harmonic of the cantilever resonance (~80–90 kHz) was used for detection. For in-plane PFM, the third harmonic frequency (~320–330 kHz) was used for detection.

Density functional perturbation theory calculations. To build the low-energy continuum model, two types of density functional perturbation theory calculations are required. For the **q**-dependent parts of the moiré dynamical matrix we calculate one single layer of MoS_2 using a 6×6×1 supercell. For the **q**-independent part, we employ 10×10 individual primitive cell bilayer MoS_2 density functional perturbation theory calculations sampling the different stackings **d**. We use Vienna Ab-initio Simulation Package with a **k**-point Monkhorst–Pack grid of 17×17×1 (3×3×1 for the supercell) with an energy cut-off of 400 eV and a unit cell height of 35 Å to provide sufficient vacuum between the layers[51,52]. For simplicity we use the local density approximation (for further details see Supplementary Discussion XII).

Calculation of strain and lattice relaxation. Strain was calculated by minimizing the total energy functional,

$$U_{\mathrm{tot}} = U_{\mathrm{B}}[\mathbf{u}^t, \mathbf{u}^b] + U_{\mathrm{E}}[\mathbf{u}^t] + U_{\mathrm{E}}[\mathbf{u}^b],$$

with respect to the top (t) and bottom (b) layer displacements $\mathbf{u}^{t/b}(\mathbf{r})$ at position $\mathbf{r}$. We model the potential energy functional U_{B} via a generalized stacking fault energy[15,25] obtained from sampling the configuration space using density functional perturbation theory. The 2D elastic energy functional $U_{\mathrm{E}}[\mathbf{u}^{t(b)}]$ is modelled using the Lamé parameters $\lambda = 3.29$ eV Å^{-2} and $\mu = 3.6$ eV Å^{-2} (ref. [15]; for further details see Supplementary Discussion I).

Data availability

All relevant data are available from the authors upon reasonable request.

Code availability

All relevant codes are available from the authors upon reasonable request.

References

51. Kresse, G. & Hafner, J. *Ab initio* molecular dynamics for liquid metals. *Phys. Rev. B* **47**, 558–561 (1993).
52. Kresse, G. & Hafner, J. *Ab initio* molecular-dynamics simulation of the liquid-metal–amorphous-semiconductor transition in germanium. *Phys. Rev. B* **49**, 251–271 (1994).

Acknowledgements

The spectroscopy experiments at the University of Texas at Austin (J.Q.) were primarily funded by the US Department of Energy, Office of Basic Energy Sciences under grant DE-SC0019398 and a grant from the University of Texas. Material preparation was funded by the Welch Foundation via grant F-1662. The collaboration between the X.L., C.-K.S., K.L. and A.H.M. groups is facilitated by the National Science Foundation Materials Research Science and Engineering Centers (MRSEC) under DMR-1720595, which funded J.C. and J.E. partially. L.L. and F.L. acknowledge support by the TU-D doctoral programme of TU Wien, as well as from the Austrian Science Fund (FWF), project I-3827, and L.L. acknowledges additional support from the Austrian Marshall Plan Foundation. We acknowledge discussions with S. Reichardt and the use of facilities and instrumentation supported by the National Science Foundation through the Center for Dynamics and Control of Materials and National Science Foundation MRSEC under cooperative agreement no. DMR-1720595. P.-H.T. and M.-L.L. acknowledge support from the National Natural Science Foundation of China (grant nos 12004377 and 11874350), CAS Key Research Program of Frontier Sciences (grant no. ZDBS-LY-SLH004) and China Postdoctoral Science Foundation (grant no. 2019TQ0317). The PFM work (D.L. and K.L.) was supported by National Science Foundation DMR-2004536 and Welch Foundation grant F-1814. X.L. gratefully acknowledges the support of sample preparations from the Welch Foundation via grant F-1662. K.W. and T.T. acknowledge support from the Elemental Strategy Initiative conducted by the MEXT, Japan, grant no. JPMXP0112101001; JSPS KAKENHI, grant no. JP20H00354; and the CREST(JPMJCR15F3), JST.

Author contributions

J.Q. led the optical experiments, and M.-L.L., C.-Y.W., W.-T.H., J.E. and J.C. assisted with the experiment. L.L. led the theoretical calculations, and J.Z. contributed to the theoretical discussions. D.L. performed the PFM measurements. J.Q. and C.Y. prepared the TBL samples. T.T. and K.W. provided the hBN sample. J.Q., L.L., F.L. and X.L. wrote the manuscript. X.L., F.L., A.H.M., P.-H.T., K.L. and C.-K.S. supervised the project. All authors discussed the results.

Competing interests

The authors declare no competing interests.

Additional information

Supplementary information The online version contains supplementary material available at https://doi.org/10.1038/s41563-021-00960-1.

Correspondence and requests for materials should be addressed to P.-H.T., F.L. or X.L.

Peer review information *Nature Materials* thanks the anonymous reviewers for their contribution to the peer review of this work.

Reprints and permissions information is available at www.nature.com/reprints.

nature portfolio

https://doi.org/10.1038/s41563-021-00960-1

Supplementary information

Phonon renormalization in reconstructed MoS_2 moiré superlattices

In the format provided by the authors and unedited

Supplemental Information:
Phonon Renormalization in Reconstructed MoS_2 Moiré Superlattices

Jiamin Quan,[1,*] Lukas Linhart,[1,2,*] Miao-Ling Lin,[3] Daehun Lee,[1] Jihang Zhu,[1] Chun-Yuan Wang,[1] Wei-Ting Hsu,[1] Junho Choi,[1] Jacob Embley,[1] Carter Young,[1] Takashi Taniguchi,[4] Kenji Watanabe,[4] Chih-Kang Shih,[1] Keji Lai,[1] Allan H. MacDonald,[1] Ping-Heng Tan,[3,†] Florian Libisch,[2,‡] and Xiaoqin Li[1,§]

[1] *Department of Physics and Center for Complex Quantum Systems, The University of Texas at Austin, Austin, TX, USA.*

[2] *Institute for Theoretical Physics, Vienna University of Technology, 1040 Vienna, Austria, EU.*

[3] *State Key Laboratory of Superlattices and Microstructures, Institute of Semiconductors, Chinese Academy of Sciences, 100083 Beijing, China*

[4] *National Institute for Materials Science, 1-1 Namiki, Tsukuba, Ibaraki 305-0044, Japan*

* These authors contributed equally to this work

† phtan@semi.ac.cn

‡ florian.libisch@tuwien.ac.at

§ elaineli@physics.utexas.edu

This PDF file includes:

I. MODELING LATTICE RELAXATION

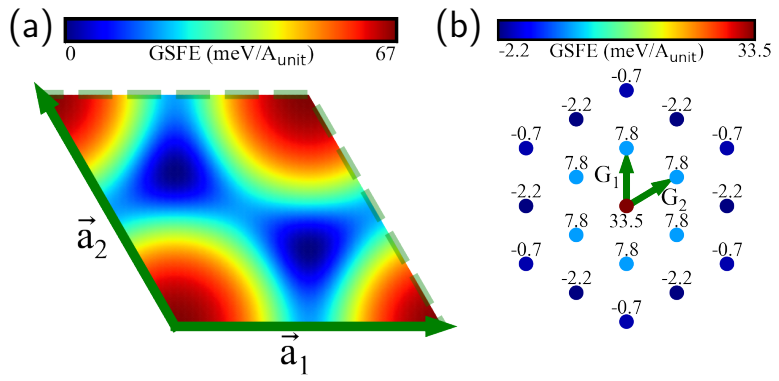

FIG. S1. Illustration of the generalized stacking fault energy (GSFE). In configuration space (a) and in reciprocal space (b).

We model lattice relaxation by solving a scheme employed for graphene bilayers by Nam et. al. [1] and generalized for MoS_2 by Carr et. al. [2]. For details we refer to their publications. The approach is based on an elasticity model which includes the second layer via an effective generalized stacking fault energy (GSFE). The total potential energy functional U_{tot} is split into an interlayer (U_B) and intralayer(elastic) (U_E) energy functional contribution and then written as [1, 3],

$$U_{tot} = U_B[\mathbf{u}^t, \mathbf{u}^b] + U_E[\mathbf{u}^t] + U_E[\mathbf{u}^b] \tag{S1}$$

with

$$U_B[\mathbf{u}^t, \mathbf{u}^b] = \int d\mathbf{r} \sum_{\mathbf{G}} c_{\mathbf{G}} \cos((\mathbf{d} + (\mathbf{u}^t - \mathbf{u}^b)) \cdot \mathbf{G}) \tag{S2}$$

$$U_E[\mathbf{u}^{\,l=t/b}] = \int d\mathbf{r} \left[\frac{\lambda+\mu}{2} \left(\frac{\partial \mathbf{u}^l_x}{\partial x} + \frac{\partial \mathbf{u}^l_y}{\partial y} \right)^2 + \frac{\mu}{2} \left(\frac{\partial \mathbf{u}^l_x}{\partial x} - \frac{\partial \mathbf{u}^l_y}{\partial y} \right)^2 + \frac{\mu}{2} \left(\frac{\partial \mathbf{u}^l_x}{\partial y} + \frac{\partial \mathbf{u}^l_y}{\partial x} \right)^2 \right]. \tag{S3}$$

Here $\lambda = 3.29$ eV/Å^2 and $\mu = 3.6$ eV/Å^2 are the Lamé parameters of pristine MoS_2[2], the $c_{\mathbf{G}}$ correspond to the Fourier coefficients as illustrated in Fig. S1b, i.e., the values, $c_{\pm\mathbf{G}_1} = c_{\pm\mathbf{G}_2} = c_{\pm(\mathbf{G}_1-\mathbf{G}_2)} = 7.8$ meV/A$_{unit}$, $c_{\pm(\mathbf{G}_1+\mathbf{G}_2)} = c_{\pm(2\mathbf{G}_1-\mathbf{G}_2)} = c_{\pm(-\mathbf{G}_1+2\mathbf{G}_2)} = -2.2$ meV/A$_{unit}$ and $c_{\pm2\mathbf{G}_1} = c_{\pm2\mathbf{G}_2} = c_{\pm(2\mathbf{G}_1-2\mathbf{G}_2)} = -0.7$ meV/A$_{unit}$. We solve for the minimal energy (Eq. S1) under variation of in-plane displacements of the top and bottom layer $\mathbf{u}^{t/b}$ using a generalized Euler-Lagrange equation. We neglect the position dependence of $\mathbf{u}(\mathbf{r})$ in the notation for brevity.

Since the two layers are equivalent we can define the relative displacement between the two layers as $\mathbf{u}^-(\mathbf{r}) = \frac{\mathbf{u}^t(\mathbf{r})}{2} = -\frac{\mathbf{u}^b(\mathbf{r})}{2}$ [1]. We assume a layer separation equal to the one calculated for the pristine configuration space by DFT, a simplification especially suited for the small twist angle regime.

The GSFE profile was obtained from the total energies of the pristine bilayer DFPT calculations (see SI. XII (B)).

Intralayer strain

We calculate local intralayer strain ϵ via the squared sum of the eigenvalues of the two-dimensional Cauchy strain

tensor as

$$\epsilon = \sqrt{\lambda_1^2 + \lambda_2^2} \qquad \text{with} \qquad \lambda_{1,2} = \mathrm{Eig}\begin{pmatrix} \frac{\partial \mathbf{u}_\mathrm{x}^{t(b)}}{\partial \mathrm{x}} & \frac{1}{2}\left(\frac{\partial \mathbf{u}_\mathrm{x}^{t(b)}}{\partial \mathrm{y}} + \frac{\partial \mathbf{u}_\mathrm{y}^{t(b)}}{\partial \mathrm{x}}\right) \\ \frac{1}{2}\left(\frac{\partial \mathbf{u}_\mathrm{x}^{t(b)}}{\partial \mathrm{y}} + \frac{\partial \mathbf{u}_\mathrm{y}^{t(b)}}{\partial \mathrm{x}}\right) & \frac{\partial \mathbf{u}_\mathrm{y}^{t(b)}}{\partial \mathrm{y}} \end{pmatrix}. \tag{S4}$$

The exact quantitative evolution of $\mathrm{E}_{2g}^{\pm}$ with strain depends on the local strain direction and the local Poisson ratio[4]. Indeed, strong local variations make an exact parametrization challenging. We have checked numerically that the qualitative predictions of our model are robust against varying definitions of strain. For simplicity, we thus use the definition of Eq. (S4).

Substrate effects on the lattice reconstruction

The lattice constants of the hBN substrate ($\mathrm{a_{hBN}}$) and MoS_2 ($\mathrm{a_{MoS_2}}$) differ by $\gtrsim 20\%$. While formally a similar configuration space energy functional as in Eq. S1 could be constructed to also account for relaxation due to the substrate (replacing the definition of $\mathbf{d}(\mathbf{r})$ with $\mathbf{d}(\mathbf{r}) = (\frac{\mathrm{a_{MoS_2}}}{\mathrm{a_{hBN}}} - 1)\mathbf{r} + \theta\hat{z} \times \mathbf{r}$ [5]), the large difference in lattice constants will cause the elastic energy to dominate the expression at any angle, leading to vanishing displacements due to the substrate GSFE. The influence of the substrate on lattice relaxation can therefore safely be neglected.

II. SCHEMATIC DIAGRAMS OF ATOMIC STACKING

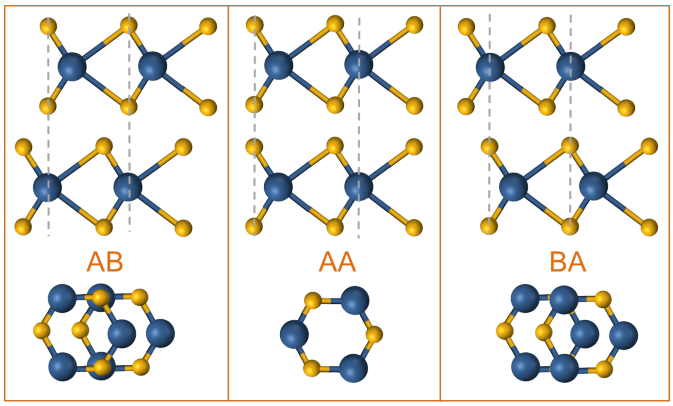

FIG. S2. Schematic diagrams of local high-symmetry stacking configurations in a TBL near a commensurate R-type stacking. Such a R-type bilayer is often referred to a bilayer with 0° twist angle.

Regions of high symmetry stacking are present in every moiré superlattice at twist angles close to 0° twist angle. We refer to these stacking areas by their pristine alignment AA, AB and BA, as illustrated in Fig. S2. AB and BA stackings are equivalent, except for an inversion along the z direction. For AB(BA) stacking, S(Mo) atoms are directly on top of Mo(S) atoms and the other Mo and S atoms are at the center of the hexagon. For AA stacking, Mo(S) atoms are directly on top of Mo(S) atoms.

III. SAMPLE PREPARATION

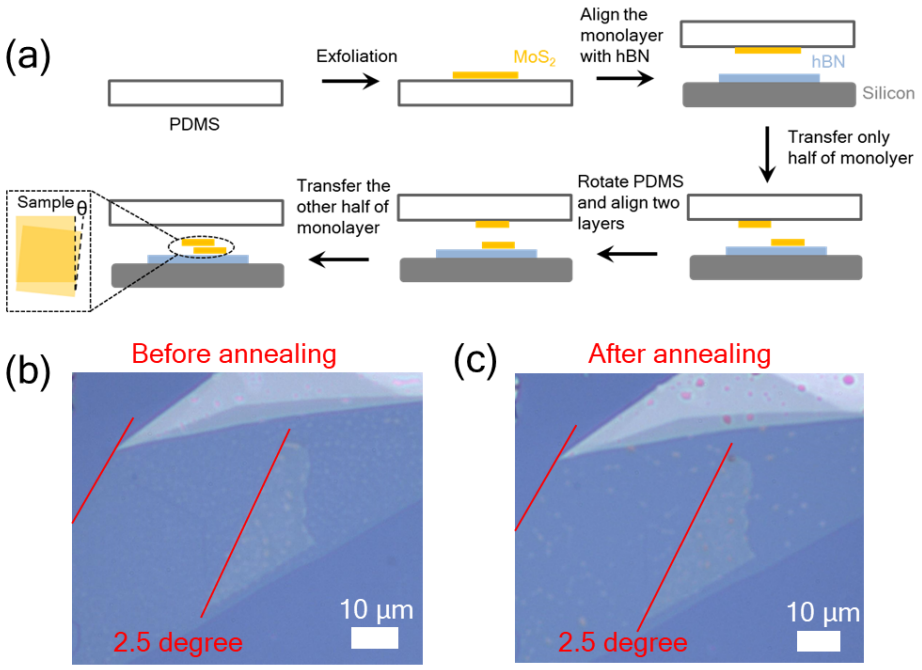

FIG. S3. (a) Schematic diagram of the sample preparation procedure. (b-c) Optical images of a sample at 2.5° twist angle (b) before and (c) after annealing. By carefully checking the sample image before and after annealing, we confirm that there is no change in twist angle during annealing for all TBLs.

IV. LOW-FREQUENCY RAMAN MAPPING

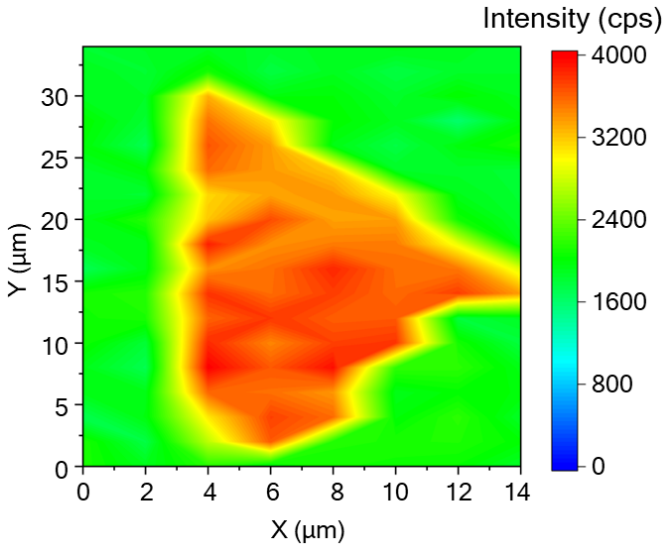

FIG. S4. The low-frequency Raman mapping of 2.5° TBL

To confirm the spatial uniformity of optical properties of the twisted bialyers, we map the low-frequency Raman spectra using a Jobin-Yvon HR800 micro-Raman system equipped with a liquid-nitrogen-cooled charge couple detector (CCD). The excitation laser was focused onto the sample using a ×100 objective lens (numerical aperture = 0.90). The excitation source is the 2.54 eV line from an Ar^+ laser. Fig. S4 shows the integrated intensity of low-frequency phonon modes of 2.5° TBL, including both the shear mode and layer breathing mode. The scan area is 14 by 34 μm with a step size of 2 μm. The small fluctuations of Raman intensity suggest the uniform interlayer coupling and high quality of the TBLs.

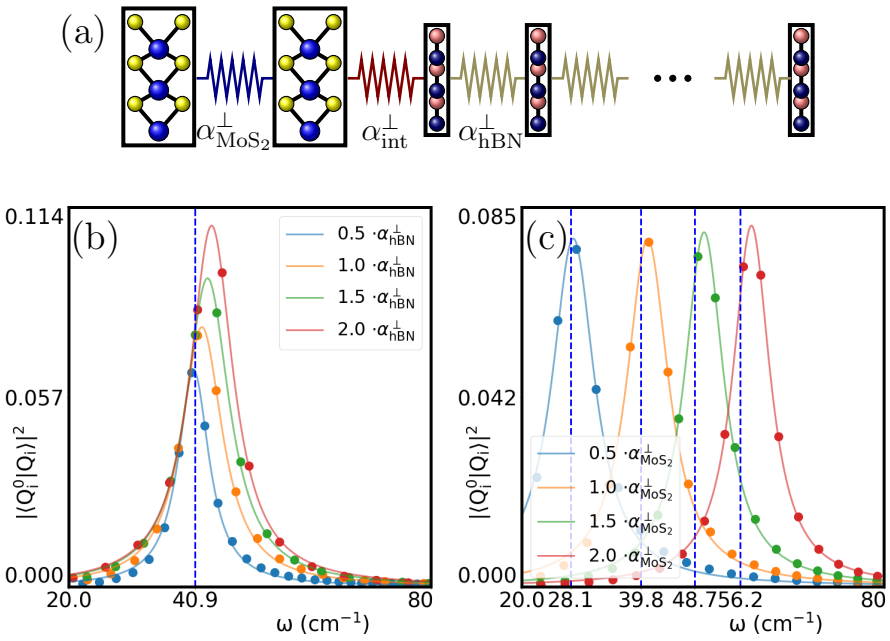

FIG. S5. (a) Linear chain model of a hBN/MoS_2 heterostructure. (b)-(c) Frequencies (ω_i) of the individual modes versus the intensity I_i (dots), when solving for the linear chain model using realistic force constants, with varying force constants. Solid lines are Lorentzian fits, resembling the envelope function. Evolution of the envelope function under a combined variation of (b) $\alpha^{\perp}_{hBN}$ and $\alpha^{\perp}_{int}$ and (c) $\alpha^{\perp}_{MoS_2}$. Dashed lines mark the corresponding LB mode frequency ω_0 of the standalone bilayer system as calculated with the linear chain model.

V. SUBSTRATE EFFECTS

Previous publications have shown that the coupling between the hBN substrate and the MoS_2 layers leads to bulk-like LB phonon modes that extend over the entire TMD/hBN heterostructure. Such extended phonons can be modeled by a linear chain model, treating each layer as a rigid entity[6] (see Fig. S5a). We use the interlayer bond polarizability model developed by Lin et al. [6] to describe the Raman response of the LB modes for our MoS_2 on hBN heterostructure. To test the robustness of our results against substrate effects we calculated the linear chain model with realistic force constants ($\alpha^{\perp}_{hBN} = 9.88 \times 10^{19}$N/m^3, $\alpha^{\perp}_{int} = 8.97 \times 10^{19}$N/m^3 and $\alpha^{\perp}_{MoS_2} = 8.9 \times 10^{19}$N/m^3)[6, 7] (see Fig. S5a). We include 39 layers of hBN (equals 12.9 nm think substrate as used in the experiment) as well as two layers of MoS_2. While the individual breathing eigenmodes $\mathbf{Q}_i$ of the heterostructure indeed extend over all layers, their intensities I_i can be mapped using the single breathing mode $\mathbf{Q}^0$ of one isolated TMD bilayer via [6]

$$I_i \propto |\langle \mathbf{Q}^0 | \mathbf{Q}_i \rangle|^2. \tag{S5}$$

The maximum of the envelope function at $\bar{\omega}$ of the resulting I_i is close to the frequency of the standalone bilayer ω^0, and describes the experimentally observed Raman intensity envelope (see SI. VI, in particular Fig. S6 and Fig. S7).

We find that $\bar{\omega}$ is slightly blue-shifted (≈1.5 cm^{-1}) compared to the standalone bilayer frequency ω_0 (compare yellow curve in Fig. S5b versus dashed blue line at 39 cm^{-1}). This might explain the systematic underestimation of LB mode frequencies calculated by DFPT. Under variations of $\alpha^{\perp}_{MoS_2}$ the frequency $\bar{\omega}$ shifts almost proportionally to the force constant, while the frequency of the corresponding standalone system ω_0 (dashed lines in Fig. S5)

follows accordingly. We find only a minimal increase in difference between $\bar{\omega}$ and ω_0.

As the hBN does not affect the lattice reconstruction of the MoS_2 layers (see SI. I), we do not expect any variation of the effective interface force constant ($\alpha_{\mathrm{int}}^{\perp}$) and hBN force constant ($\alpha_{\mathrm{hBN}}^{\perp}$) with twist angle. Nevertheless we tested the dependence of the envelope function center under variations of $\alpha_{\mathrm{hBN}}^{\perp}$ and $\alpha_{\mathrm{int}}^{\perp}$. We find that $\bar{\omega}$ is robust against individual and combined variations of α_{hBN} and α_{int}. Variations in the range of $0.5 \times \alpha_{\mathrm{i}} - 2 \times \alpha_{\mathrm{i}}$ result in shifts of $\bar{\omega}$ smaller than 2 cm^{-1} (see Fig. S5b).

In conclusion, the substrate couples strongly to the MoS_2 layers, but the central frequencies of the intensity envelope of the bulk-like LB phonons map the LB mode frequency of the corresponding standalone TMD TBL (shifted by ≈ 1.5 cm^{-1}). The twist angle dependent frequency evolution of the LB mode only depends on the twist angle dependent effective force constant between the TMD TBLs.

VI. DATA ANALYSIS

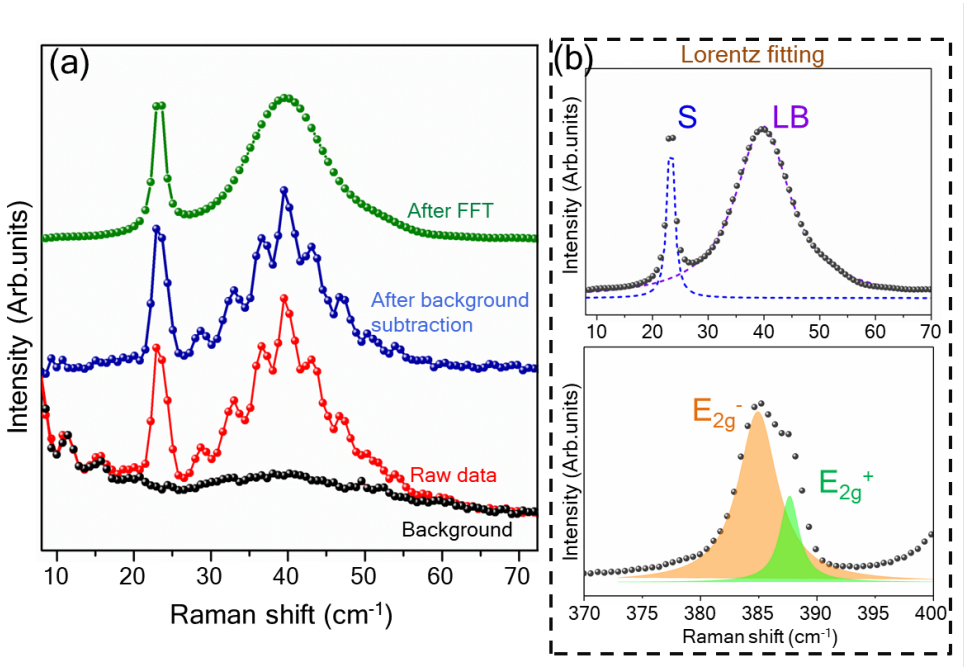

FIG. S6. (a) Data processing of the low-frequency Raman spectra from the sample with 0° twist angle in the main text. (b) The Lorentz fitting of both low-frequency (0° sample) and high-frequency (2.5° TBL) modes.

The low-frequency Raman data shown in the main text is not the raw data directly obtained from our measurements. The raw data includes oscillatory signals originating from the coupling between the TMD TBLs and the hBN substrate. Such oscillatory signal distracts from the main features relevant to the moiré pattern. We perform fast Fourier transformation (FFT) to remove such oscillations, which are most prominently visible on the LB modes. In this section we carefully document this data processing for reader's reference. We present Raman spectra from the 0° TBL as an example.

We first remove the background by subtracting data taken from the monolayer region. The Raman spectrum features a sharp S mode and a broad LB mode (see Fig. S6a). Oscillatory signals on the LB mode originate from the coupling between 2D electrons confined to the MoS_2 TBL and the bulk-like LB phonons extending over the entire vdW heterostructures (vdWHs) as has been previously investigated [6]. We apply a FFT processing to filter out the oscillatory signal before performing a detailed analysis. To confirm that the FFT processing does not affect the experimental values, we extract the central frequencies and linewidths before and after the FFT analysis on various samples. For example, we confirm that the central frequency 39.7 cm^{-1} and the full-width-half-maximum of 11.7 cm^{-1} in the 0° TBL do not change due to the FFT. Further discussion about the hBN substrate effect can be found in the last section.

All the Raman modes are fitted by Lorentz functions (using the software "origin 2017") (Fig. S6b). The error bars of Figs. 3 and S8 are calculated via the mean residual variance (Chi-Sqr) of the fitting parameter using the "Origin" software.The low-frequency Raman spectra after FFT processing are well fitted by two Lorentzian functions (Fig. S6b top), which correspond to the S mode and LB mode, respectively. We also present Lorentzian

fitting to the high-frequency E_{2g} mode, which splits into two Lorentz lines (E_{2g}^{+} and E_{2g}^{-} mode) due to the strain effect in the 2.5° TBL (Fig. S6b bottom). It should be noted that splited E_{2g} modes can't be identified by polarized Raman measurements due to the directionless of moiré strain.

VII. RAMAN SPECTRA BEFORE FFT PROCESSING

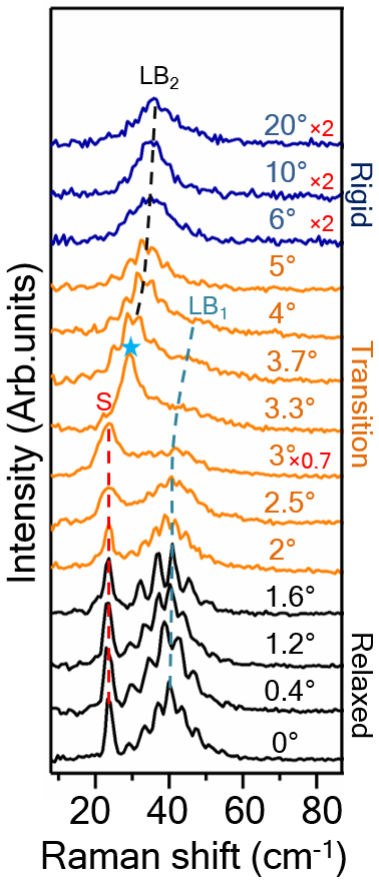

FIG. S7. Low-frequency Raman spectra before the FFT processing as a function of twist angle. The fringes originate from the coupling between the TBLs and hBN substrate. The coupling strength changes with the twist angle.

The S and LB modes are distinguished via polarized Raman spectroscopy. The undefined mode in the TBL at 3.3° (cyan star) in Fig. 3a-b of the main text cannot be detected in the cross polarization (HV), which is typical of a LB mode. However, this peak is smooth and has no oscillatory signals. As reported in our previous work[8], LB modes of MoS_2 TBLs should efficiently interact with the LB modes in the hBN due to the strong interfacial coupling between the hBN and TBLs (see SI. V), resulting in bulk-like collective LB vibrations of entire layers in the vdWHs. Due to these conflicting properties of this mode, we refrain from assigning this mode in the 3.3° TBL.

VIII. THE LINEWIDTH OF THE E_{2g} MODE

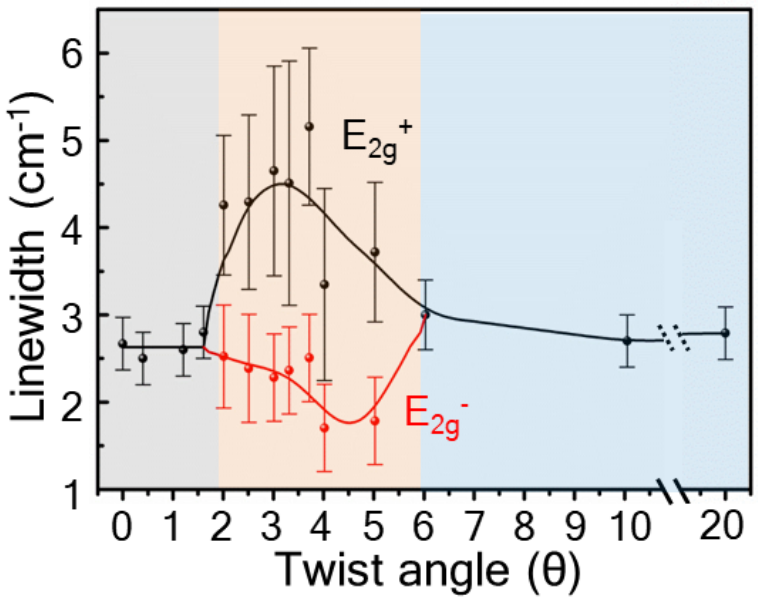

FIG. S8. The linewidth of the split E_{2g} modes as a function of twist angle. The error bars represent the uncertainty of the fitting parameter in the fitting process.

In Fig. S8, the linewidth of E_{2g}^{+} first increases and then decreases as a function of the twist angle within the transition regime, while the E_{2g}^{-} mode shows an opposite evolution. The linewidth of the E_{2g}^{+} broadens by a maximal value of 2.7 cm^{-1} relative to the rigid/relaxed regime. The large error bars in the transition regime are ascribed to fitting errors.

IX. BREATHING AND SHEAR MODE INTENSITY

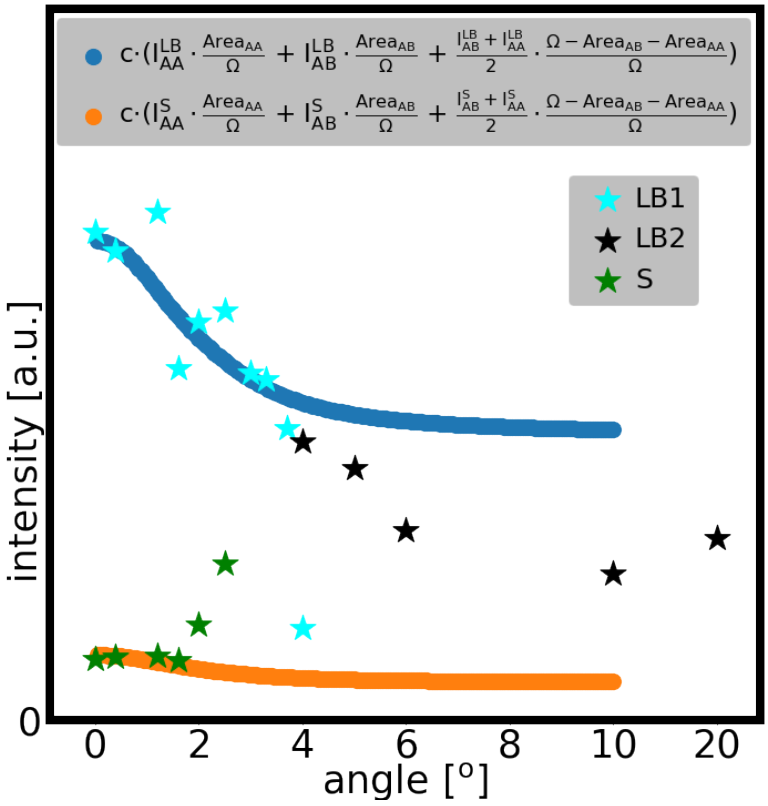

FIG. S9. S and LB mode intensities as a function of twist angle. The stars indicate the experimental LB and S mode intensities. The solid lines are the S and LB mode evolution weighting the relative variations of the AA and AB(BA) stacking area as a function of strain. $I^{S}_{AA(AB)} = 0.0(5.36)$ [a.u.] and $I^{LB}_{AA(AB)} = 1.44(39.25)$ [a.u.] are the DFPT calculated Raman intensities at the high symmetry stacking configurations as calculated in [9]. c is an arbitrary scaling factor, equal for the S and LB mode. We do not include the change of the corrugation in the estimation for the intensity, relevant at $\theta > 4°$. The twist angle dependent relative areas $\frac{Area_{AB}}{\Omega}$ and $\frac{Area_{AA}}{\Omega}$ are plotted in Fig. 1e of the main text.

Experimental S and LB mode intensities as a function of the twist angle and their theoretical interpretation are illustrated in Fig. S9. The LB and S mode intensities depend on the relative stacking configuration. In the simplest approximation, LB and S mode intensities in a moiré crystal can be modeled by weighting the commensurate stacking LB and S mode intensities $I^{LB(S)}_{AB(AA)}$ by their areas within the moiré supercell. The AB(BA) stacking configuration dominates at small twist angles ($Area_{AB} \gg Area_{AA}$), therefore the observed intensities are similar to I_{AB}. With increasing twist angle the intensities of the LB and S modes should decrease as the relative weight of the AA area increases and $I_{AB} > I_{AA}$ for both modes. While this prediction fits with the measured LB mode intensities (see Fig. S9), the data for the S mode instead shows an increase in intensity close to $\theta \approx 3°$. Considering only the relative areas of the different stacking configurations neglects changes in corrugation and therefore significantly deviates from experiment at $\theta > 3°$. Including the reduction in corrugation at a large enough twist angle ($\approx 3°$), we expect a strong reduction in S mode (and LB mode) intensity (Fig. S10 c), in line with the observed disappearance of the S mode (see Fig. S9 and [9]), as $I^{S}_{AA} \approx 0$.

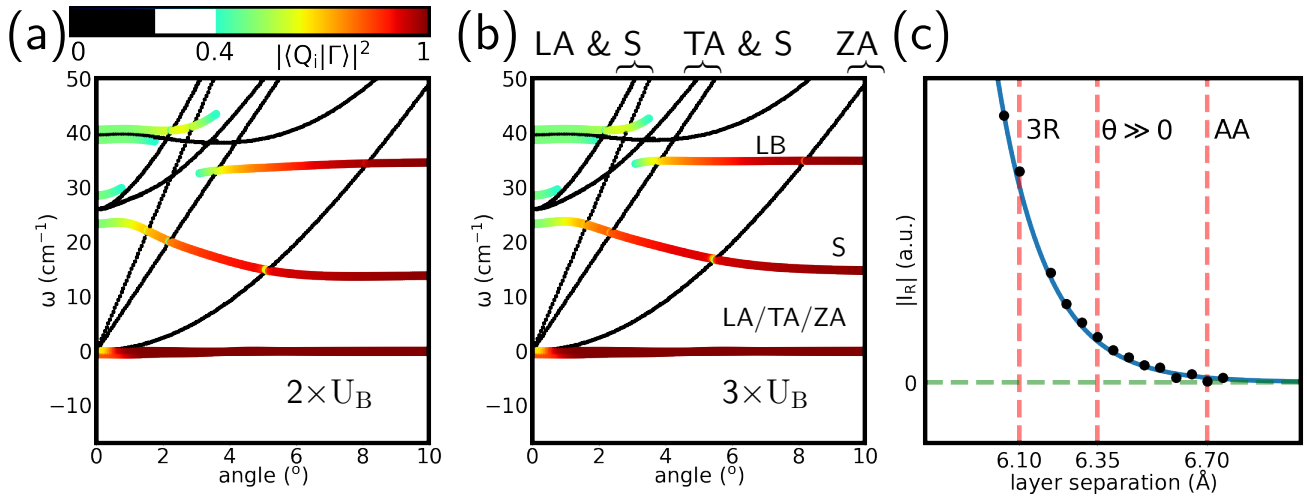

FIG. S10. Understanding the S mode evolution. (a) and (b) illustrate the low energy phonon evolution similar to Fig. 4e in the main text when the GSFE is doubled (a) or tripled (b). The reduced anti-crossing of the breathing mode at $\approx 3.5°$ compared to the main text can be understood from lattice reconstruction. With larger lattice reconstruction in the transition region, the coupling element configuration representation becomes less harmonic and the first shell continuum model approximation becomes less valid. Including more shells opens the avoided crossing to a size as in the main text (not shown). (c) Calculated intensity evolution of the S mode in an AB(BA) stacking configuration as a function of layer separation, calculated as outlined in SI. XII C. The dashed red lines indicate the equilibrium layer separation at the corresponding stacking configurations (3R and AA) as well as the uniform layer separation at large twist angles[9].

X. DETAILED ANALYSIS OF THE SHEAR MODE EVOLUTION

While theory and experiment agree very well concerning the evolution of the breathing modes, our calculations incorrectly predict a drop in shear mode frequency at intermediate twist angles. To elucidate the reason for this discrepancy, we note that we neglect the dependence of the corrugation amplitude on twist angle. For small twist angles (relaxed regime), the various stacking regions (AA vs. AB(BA)) can be viewed as completely independent. AA as well as AB(BA) stacking configurations are approximately at their equilibrium layer separation[9] ($\Delta_{AA} \approx 6.7$Å and $\Delta_{AB} = \Delta_{BA} \approx 6.1$Å). In the transition regime (with increased twist angle, i.e. reduced super cell size), the stacking configurations move closer to each other and therefore the corrugation $\Delta = \Delta_{AA} - \Delta_{AB}$ is reduced and the layers become flat, with a uniform spacing of $\Delta_{AA} \approx \Delta_{AB} \approx 6.35$Å in the large angle limit [9]. The influence of this reduction of Δ affects both (i) the S mode frequency and (ii) its intensity. We first consider the frequency (i). A reduced corrugation causes Δ_{AA} to decrease and Δ_{AB} to increase. These changes increase the differences in GSFE between AA and AB regions due to its exponential sensitivity on layer separation (the stacking dependent energy difference in Fig. S1 increases). A larger GSFE difference will increase strain in the system (an observation that also matches the evolution of the optical mode). This contribution will shift the point at which the relative weight of the AB(BA) area starts to decline to a larger twist angle, causing the S mode to stay approximately constant up to a larger twist angle (see Fig. S10a and b). By contrast, without considering the effect of reduced corrugation at intermediate twist angles on the GSFE, the S mode frequency starts to decrease at a smaller twist angle ($\approx 1.5°$) due to the decrease of the relative weight of the AB/BA regions as seen in our calculations (see Fig. 4e).

Concerning the S mode intensity (ii), we note that the optical intensity of the S mode stems almost entirely from the AB stacking configuration, as the change in polarizability for the S mode is maximal at the smallest layer separation (as noted by [9]). With larger Δ_{AB} for larger twist angles, the change in polarizability with infinitesimal atom displacements exponentially decays and so does the optical intensity[10] of the S mode (see Fig. S10c).

In summary the S mode has approximately constant energy also for angles reaching into the transition regime (up to $\approx 3°$) due to increased GSFE stemming from larger strain. Furthermore the S mode vanishes in the rigid regime due to reduced corrugation and therefore reduced optical intensity.

XI. LOW ENERGY CONTINUUM MODEL FOR ACOUSTIC PHONONS AT THE Γ POINT

Our low-energy continuum model for phonons is adopted from the model for the electronic system introduced by J. Jung et al. [5]. We discuss the derivation of the model for completeness and to highlight its usability for calculating phonons.

A. Derivation of the moiré dynamical matrix $\bar{D}_m$

The dynamical matrix $\bar{D}$ of a Bloch periodic system in the harmonic approximation can be constructed from the Hessian matrix $\bar{H}$ via

$$D^{\alpha,\beta}_{\mathrm{I,J}}(\mathbf{q}) = \frac{1}{\sqrt{\mathrm{M_I M_J}}} \sum_{\mathbf{R}-\mathbf{R}'} e^{i\mathbf{R}\cdot\mathbf{q}} \cdot \mathrm{H}^{\alpha,\beta}_{\mathrm{I,J}}(\mathbf{R}-\mathbf{R}') \cdot e^{-i\mathbf{R}'\cdot\mathbf{q}}. \tag{S6}$$

where I(J) refers to the atomic index in the pristine bilayer unit cell with an atom of mass $\mathrm{M_{I(J)}}$ and $\alpha(\beta)$ to the three Cartesian degrees of freedom. Furthermore $\mathbf{R}(')$ are the positions of the corresponding pristine unit cell, spanned by a linear combination of pristine unit vectors $\mathbf{a}_i$. We define the pristine unit vectors via, $\mathbf{a}_1 = a_0(1,0)$ and $\mathbf{a}_2 = a_0(-1/2, \sqrt{3}/2)$, with the lattice constant $a_0 = 3.125$ Å.

In the next step we assume that within a moiré system H depends only on the local stacking configuration of the two layers. For the case of MoS_2 TBL, with a small rotation angle, the relation between configuration space $\mathbf{d}$ and a position $\mathbf{r}$ can then - within the first moiré length - be approximated by $\mathbf{d}(\mathbf{r}) \approx \theta\hat{z} \times \mathbf{r}$ and does not change over the range of one pristine unit cell ($\mathbf{d}(\mathbf{r}) \approx \mathbf{d}(\mathbf{R})$). Consequently H is now a function of $\mathbf{R}$ and not only of $\mathbf{R}-\mathbf{R}'$ as in the Bloch periodic case and therefore not diagonal in reciprocal space anymore,

$$D^{\alpha,\beta}_{\mathrm{I,J}}(\mathbf{q},\mathbf{q}') = \frac{1}{\sqrt{\mathrm{M_I M_J}}} \sum_{\mathbf{R},\mathbf{R}'} e^{i\mathbf{R}\cdot\mathbf{q}} \cdot \mathrm{H}^{\alpha,\beta}_{\mathrm{I,J}}(\mathbf{R}-\mathbf{R}'|\mathbf{d}(\mathbf{R})) \cdot e^{-i\mathbf{R}'\cdot\mathbf{q}'}. \tag{S7}$$

Since $\mathbf{d}(\mathbf{r})$ is periodic on the moiré length $\mathbf{d}(\mathbf{r}) = \mathbf{d}(\mathbf{r}+\mathbf{a}_M)$ and the pristine lattice vector $\mathbf{a}$ is related to moiré lattice vector $\mathbf{a}_M$ by $\mathbf{a} \approx \theta\hat{z}\times\mathbf{a}_M$, we have $\mathrm{H}^{\alpha,\beta}_{\mathrm{I,J}}(\mathbf{R}-\mathbf{R}'|\mathbf{d}(\mathbf{R})) \approx \mathrm{H}^{\alpha,\beta}_{\mathrm{I,J}}(\mathbf{R}-\mathbf{R}'|\mathbf{d}(\mathbf{R})+\mathbf{a})$, which allows the expansion in terms of pristine reciprocal lattice vectors $\mathbf{G}$,

$$\mathrm{H}^{\alpha,\beta}_{\mathrm{I,J}}(\mathbf{R}-\mathbf{R}'|\mathbf{d}(\mathbf{R})) = \sum_{\mathbf{G}} \mathrm{H}^{\alpha,\beta}_{\mathrm{I,J}}(\mathbf{R}-\mathbf{R}'|\mathbf{G}) \cdot e^{-i\mathbf{d}(\mathbf{R})\cdot\mathbf{G}}. \tag{S8}$$

Substituting Eq. S8 into Eq. S7 as well as inserting an additional $\mathbb{1}$ yields,

$$D^{\alpha,\beta}_{\mathrm{I,J}}(\mathbf{q},\mathbf{q}') = \frac{1}{\sqrt{\mathrm{M_I M_J}}} \sum_{\mathbf{R},\mathbf{R}'} \sum_{\mathbf{G}} \mathrm{H}^{\alpha,\beta}_{\mathrm{I,J}}(\mathbf{R}-\mathbf{R}'|\mathbf{G}) \cdot e^{i\mathbf{R}\cdot\mathbf{q}} \cdot \underbrace{e^{i\mathbf{R}\cdot\mathbf{q}'} \cdot e^{-i\mathbf{R}\cdot\mathbf{q}'}}_{\mathbb{1}} \cdot e^{-i\mathbf{R}'\cdot\mathbf{q}'} \cdot e^{-i\mathbf{R}\cdot\tilde{\mathbf{G}}} \tag{S9}$$

using $\mathbf{d}(\mathbf{R})\cdot\mathbf{G} = \theta\hat{z}\times\mathbf{R}\cdot\mathbf{G} = -\theta\hat{z}\times\mathbf{G}\cdot\mathbf{R} = \tilde{\mathbf{G}}\cdot\mathbf{R}$. Substituting $\mathbf{R}'' = \mathbf{R}-\mathbf{R}'$ and using the pristine cell periodicity of $\mathrm{H}^{\alpha,\beta}_{\mathrm{I,J}}(\mathbf{R}-\mathbf{R}'|\mathbf{G})$ allows writing

$$D^{\alpha,\beta}_{\mathrm{I,J}}(\mathbf{q},\mathbf{q}') = \frac{1}{\sqrt{\mathrm{M_I M_J}}} \sum_{\mathbf{R},\mathbf{R}''} \sum_{\mathbf{G}} \mathrm{H}^{\alpha,\beta}_{\mathrm{I,J}}(\mathbf{R}''|\mathbf{G}) \cdot e^{i\mathbf{R}\cdot(\mathbf{q}-\mathbf{q}'-\tilde{\mathbf{G}})} \cdot e^{i\mathbf{R}''\cdot\mathbf{q}'} \tag{S10}$$

which can be further simplified to

$$D^{\alpha,\beta}_{\mathrm{I,J}}(\mathbf{q},\mathbf{q}') = \sum_{\mathbf{R}} \sum_{\mathbf{G}} \cdot e^{i\mathbf{R}\cdot(\mathbf{q}-\mathbf{q}'-\tilde{\mathbf{G}})} \underbrace{\frac{1}{\sqrt{\mathrm{M_I M_J}}} \sum_{\mathbf{R}''} \mathrm{H}^{\alpha,\beta}_{\mathrm{I,J}}(\mathbf{R}''|\mathbf{G}) e^{i\mathbf{R}''\cdot\mathbf{q}'}}_{\mathrm{D}^{\alpha,\beta}_{\mathrm{I,J}}(\mathbf{q}'|\mathbf{G})}. \tag{S11}$$

We finally end up with a surprisingly simple expression for the dynamical matrix of twisted bilayer MoS_2, now omitting the atomic and Cartesian coordinates and indicating the matrix form via a bar. Furthermore we identify the resulting dynamical matrix $\bar{D}$ as the moiré dynamical matrix

$$\bar{D}_{\mathrm{m}}(\mathbf{q},\mathbf{q}') = \sum_{\mathbf{G}} \delta(\mathbf{q}-\mathbf{q}'-\tilde{\mathbf{G}}) \cdot \bar{D}(\mathbf{q}'|\mathbf{G})). \tag{S12}$$

Since we want to compare our calculations with Raman measurements, we are interested in the phonon energies close to the $\mathbf{\Gamma}$ point. For small θ it holds that $|\tilde{\mathbf{G}}| \ll |\mathbf{G}|$ and we can approximate $\bar{D}(\mathbf{q}|\mathbf{G}\neq\mathbf{0}) \approx \bar{D}(\mathbf{\Gamma}|\mathbf{G}\neq 0)$, with the only $\mathbf{q}$ dependence in the dynamical matrix components where $\bar{D}(\mathbf{q}|\mathbf{G}=0)$. This $\mathbf{G}=0$ component can be further split into an intralayer $l(\mathrm{I}) = l(\mathrm{J})$ and interlayer $l(\mathrm{I}) \neq l(\mathrm{J})$ part, where we again approximate $\bar{D}_{\mathrm{inter}}(\mathbf{q}|\mathbf{0}) \approx \bar{D}_{\mathrm{inter}}(\mathbf{\Gamma}|\mathbf{0})$. Approximations involving $\mathbf{q}\to\mathbf{\Gamma}$ become exact at the $\mathbf{\Gamma}$-point. In the last approximation we exploit that $|\bar{D}(\mathbf{q}|\mathbf{G})|$ quickly decays to zero with increasing $|\mathbf{G}|$. In fact, we find that already the six first neighboring $\mathbf{\Gamma}$-points, $\{\mathbf{G}_1,\mathbf{G}_2,\mathbf{G}_3,\mathbf{G}_4,\mathbf{G}_5,\mathbf{G}_6\}$ are sufficient, allowing to truncate the reciprocal expansion after the first "shell" for small energies.

The final moiré dynamical matrix at the $\mathbf{\Gamma}$-point for small twist angles can be written as,

$$\bar{D}_{\mathrm{m}}(\mathbf{q}) \approx \begin{pmatrix} \bar{D}(\mathbf{q}|\mathbf{0}) & \bar{D}(\mathbf{\Gamma}|\mathbf{G}_1) & \bar{D}(\mathbf{\Gamma}|\mathbf{G}_2) & \bar{D}(\mathbf{\Gamma}|\mathbf{G}_3) & \bar{D}(\mathbf{\Gamma}|\mathbf{G}_4) & \bar{D}(\mathbf{\Gamma}|\mathbf{G}_5) & \bar{D}(\mathbf{\Gamma}|\mathbf{G}_6) \\ \bar{D}^{\dagger}(\mathbf{\Gamma}|\mathbf{G}_1) & \bar{D}(\mathbf{q}+\tilde{\mathbf{G}}_1|\mathbf{0}) & & & & & \\ \bar{D}^{\dagger}(\mathbf{\Gamma}|\mathbf{G}_2) & & \bar{D}(\mathbf{q}+\tilde{\mathbf{G}}_2|\mathbf{0}) & & & & \\ \bar{D}^{\dagger}(\mathbf{\Gamma}|\mathbf{G}_3) & & & \bar{D}(\mathbf{q}+\tilde{\mathbf{G}}_3|\mathbf{0}) & & & \\ \bar{D}^{\dagger}(\mathbf{\Gamma}|\mathbf{G}_4) & & & & \bar{D}(\mathbf{q}+\tilde{\mathbf{G}}_4|\mathbf{0}) & & \\ \bar{D}^{\dagger}(\mathbf{\Gamma}|\mathbf{G}_5) & & & & & \bar{D}(\mathbf{q}+\tilde{\mathbf{G}}_5|\mathbf{0}) & \\ \bar{D}^{\dagger}(\mathbf{\Gamma}|\mathbf{G}_6) & & & & & & \bar{D}(\mathbf{q}+\tilde{\mathbf{G}}_6|\mathbf{0}) \end{pmatrix} \tag{S13}$$

or one matrix block more explicitly,

$$\bar{D}_m(\mathbf{q}) \approx \begin{pmatrix} \bar{D}^{\mathrm{t}}_{\mathrm{intra}}(\mathbf{q}|0) & \bar{D}_{\mathrm{inter}}(\mathbf{\Gamma}|0) & \dots \\ \bar{D}^{\dagger}_{\mathrm{inter}}(\mathbf{\Gamma}|0) & \bar{D}^{\mathrm{b}}_{\mathrm{intra}}(\mathbf{q}|0) & \dots \\ \vdots & \vdots & \ddots \end{pmatrix}. \tag{S14}$$

Note that the only explicit angle dependence of Eq. S13 is incorporated in the $\tilde{\mathbf{G}}$ dependence of the diagonal blocks. Only when accounting for lattice relaxation, the dynamical matrix components become implicitly angle dependent (see mapping in Eq. S17). We neglect coupling between the first shell moiré $\mathbf{\Gamma}$ points, present in Eq. 1, in the main text, for the sake of simplicity. Its effect on the modes residing at the central $\mathbf{\Gamma}$ point is small, as we have verified numerically. To correct for the well-known approximations within DFT we include one scaling factor of 1.15 to the interlayer dynamical matrix component $\bar{D}_{\mathrm{inter}}(\mathbf{\Gamma}|0)$ to match the measured phonon energies at $\theta = 0$.

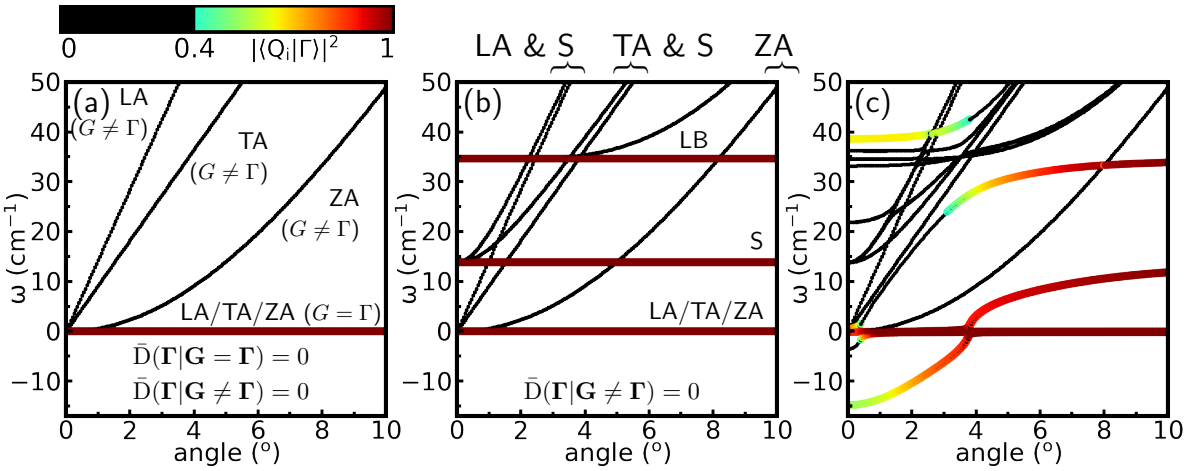

FIG. S11. Illustration of the angle dependent phonon frequencies at the central $\mathbf{\Gamma}$-point, when the various moiré $\mathbf{\Gamma}$-points $(\mathbf{\Gamma}, \mathbf{\Gamma} + \tilde{\mathbf{G}}_1, ...)$ are not coupled, i.e. when $\bar{D}(\mathbf{\Gamma}, \mathbf{G} \neq 0) = 0$. (a) if additionally $\bar{D}_{\mathrm{inter}}(\mathbf{\Gamma}, \mathbf{G} = \mathbf{0}) = 0$ and (b) when including these terms. The color code indicates the projection of the phonon Eigenmode $\mathbf{Q}_\mathrm{i}$ onto the central $\mathbf{\Gamma}$-point, black lines indicate the phonon energies of modes residing at the moiré $\mathbf{\Gamma}$-points $(\mathbf{\Gamma} + \tilde{\mathbf{G}}_i)$. The morié $\mathbf{\Gamma}$-points are shifted away from the central $\mathbf{\Gamma}$-point with increasing angle, since $\tilde{\mathbf{G}} \propto \theta$. Therefore the band evolution of phonons residing at these moiré $\mathbf{\Gamma}$-point evaluated at the central $\mathbf{\Gamma}$-point, resemble the phonon band structure of the single-layer (a) and the coupling-averaged bilayer band structure (compare also to Fig. S13b). (c) As Fig. 4d in the main text.

B. Adaptions to the acoustic sum rule

To account for the coupling between $\mathbf{q}$ off-diagonal components the acoustic sum rule has to be sightly adapted to

$$D^{\alpha,\beta}_{\mathrm{m,I,I}}(\mathbf{\Gamma}|\mathbf{0}) = D^{\alpha,\beta}_{\mathrm{m,I,I}}(\mathbf{\Gamma}|\mathbf{0}) - \sum_{\mathbf{G}_i} \sum_{\mathrm{J} \neq \mathrm{I}} D^{\alpha,\beta}_{\mathrm{m,I,J}}(\mathbf{\Gamma}|\mathbf{G}) \cdot \sqrt{\frac{\mathrm{M^J}}{\mathrm{M^I}}}. \tag{S15}$$

This form ensures that the sum of all forces acting on individual atoms vanishes in all directions also when including dynamical matrix components with $\mathbf{G} \neq \mathbf{0}$. The calculated results of the dispersions for LB, S modes and the acoustic phonon are shown in Fig. S11.

C. Evaluating $\bar{D}(\mathbf{\Gamma}, \mathbf{G})$, including strain

We recognize that

$$\bar{D}(\mathbf{\Gamma}|\mathbf{G}) = \sum_{\mathbf{d}} \bar{D}(\mathbf{\Gamma}|\mathbf{d}) \cdot e^{i\mathbf{d}\cdot\mathbf{G}}, \tag{S16}$$

and can straightforwardly calculate $\bar{D}(\mathbf{\Gamma}, \mathbf{d})$ from DFT. Via the method introduced in SI. I one can calculate the displacement $\mathbf{u}^-(\mathbf{r})$ between the two layers, allowing to map the configuration space onto the distorted configuration space $\mathbf{d} \to \mathbf{d} + \mathbf{u}^-(\mathbf{r})$. With this, one can write

$$\bar{D}(\mathbf{\Gamma}, \mathbf{d}) \to \bar{D}(\mathbf{\Gamma}, \mathbf{d} + \mathbf{u}^-(\mathbf{r}(\mathbf{d}))) \Rightarrow \bar{D}(\mathbf{\Gamma}, \mathbf{d}, \theta), \tag{S17}$$

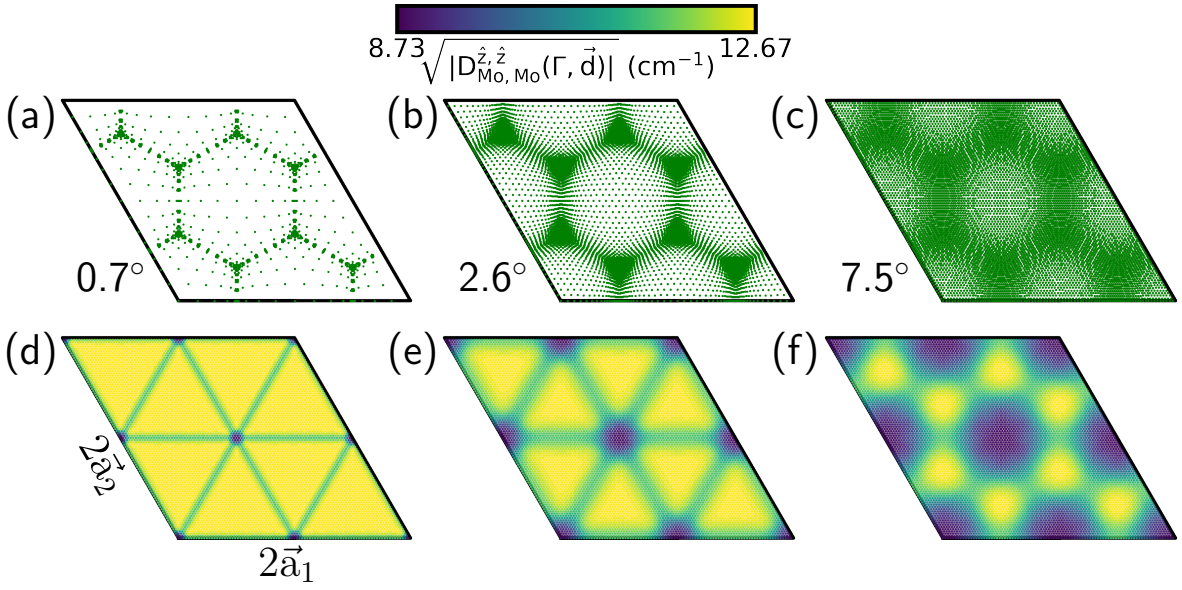

FIG. S12. Illustration of strain influence on one component of the dynamical matrix $D^{\hat{z},\hat{z}}_{\mathrm{Mo,Mo}}(\mathbf{\Gamma},\mathbf{d},\theta)$ as a function of twist angle. (a)-(c) Distortion due to strain of a regular grid sampling the configuration space for 0.7°, 2.6° and 7.5° degrees twist angle. (d)-(f) Evolution of the angle dependent dynamical matrix component $D^{\hat{z},\hat{z}}_{\mathrm{Mo,Mo}}(\mathbf{\Gamma},\mathbf{d},\theta)$ as calculated via (Eq. S17). For small twist angles (e.g. 0.7°), the dynamical matrix component is almost entirely built from AB(BA) stacking components, while the large angle limit (7.5°) resembles an almost unstrained dynamical matrix component.

since $\mathbf{u}^-$ is an angle dependent quantity, the mapping of Eq. S17 as well as the Fourier transform of Eq. S16 has to be performed for each angle θ independently. The effects of the strain mapping on the components of the dynamical matrix elements is illustrated in Fig. S12. While the dynamical matrix components remain mostly unaffected at large angles, small angles result in dynamical matrix elements that are almost entirely dominated by AB(BA) stacking in configuration space. Therefore, this remapping causes the entire moiré lattice to become stable, i.e. removes all imaginary frequencies present in the calculation without lattice relaxation (compare Fig. 4(e) of the main text).

D. Real space interpretation of phonon modes

The individual phonon eigenmodes $\mathbf{Q}_{\mathrm{i}}(\mathbf{r})$ in real space can be obtained from the moiré dynamical matrix equation,

$$\omega^2_{\mathrm{i}}(\mathbf{\Gamma})\mathbf{Q}_{\mathrm{i},\tilde{\mathbf{G}}} = \sum_{\tilde{\mathbf{G}}'} \bar{D}_{\mathrm{m}}(\mathbf{\Gamma},\mathbf{\Gamma}+\tilde{\mathbf{G}}')\mathbf{Q}_{\mathrm{i},\tilde{\mathbf{G}}'} \tag{S18}$$

via

$$\mathbf{Q}_{\mathrm{i}}(\mathbf{r}) = \sum_{\tilde{\mathbf{G}}} \mathbf{Q}_{\mathrm{i},\tilde{\mathbf{G}}} e^{-i\tilde{\mathbf{G}}\cdot\mathbf{r}}, \tag{S19}$$

allowing to calculate the displacement of each eigenmode $\mathbf{Q}_{\mathrm{i}}$ at position $\mathbf{r}$ within the quasi supercell. The phonon eigenmodes of the LB_1 and LB_2 modes at the twist angle of the anti-crossing (3.5°) are rather complex (Fig. S14). Yet, they are complementary to each other and the LB modes have a significant in-plane component.

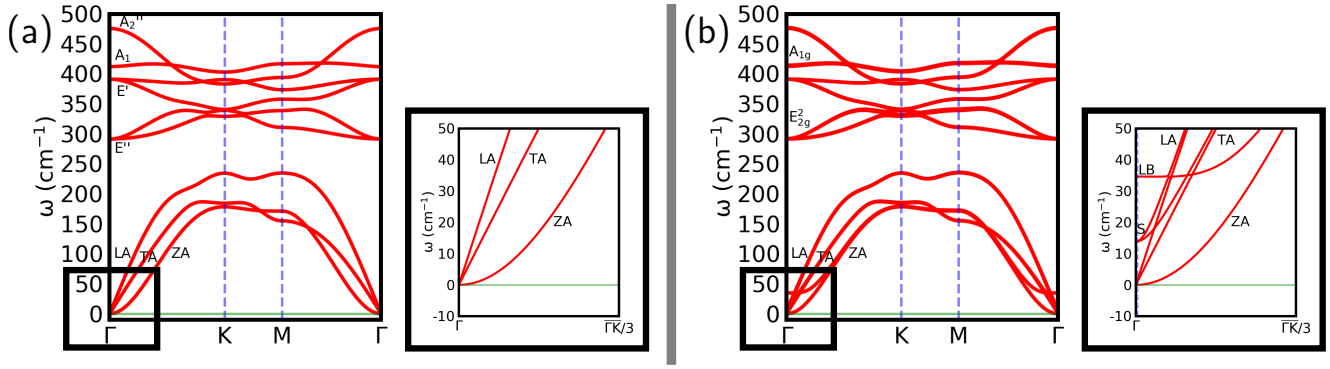

FIG. S13. Phonon band structures of single layer and effective bilayer MoS_2, with mode assignment as in[11]. (a) The phonon band structure of single layer MoS_2 as calculated from DFPT. (b) The phonon band structure of an effective bilayer MoS_2, calculated using $\bar{D}(\mathbf{q}|0)$. In such an effective bilayer the interlayer dynamical matrix elements $\mathrm{D}^{\alpha,\beta}_{\mathrm{I,J,inter}}(\mathbf{q}, \mathbf{G} = 0)$ are not $\mathbf{q}$-dependent, i.e. $\bar{D}_{\mathrm{inter}}(\mathbf{q}, \mathbf{G} = 0) \approx \bar{D}_{\mathrm{inter}}(\mathbf{\Gamma}, \mathbf{G} = 0)$ (see also Eqs. S13-S14)

.

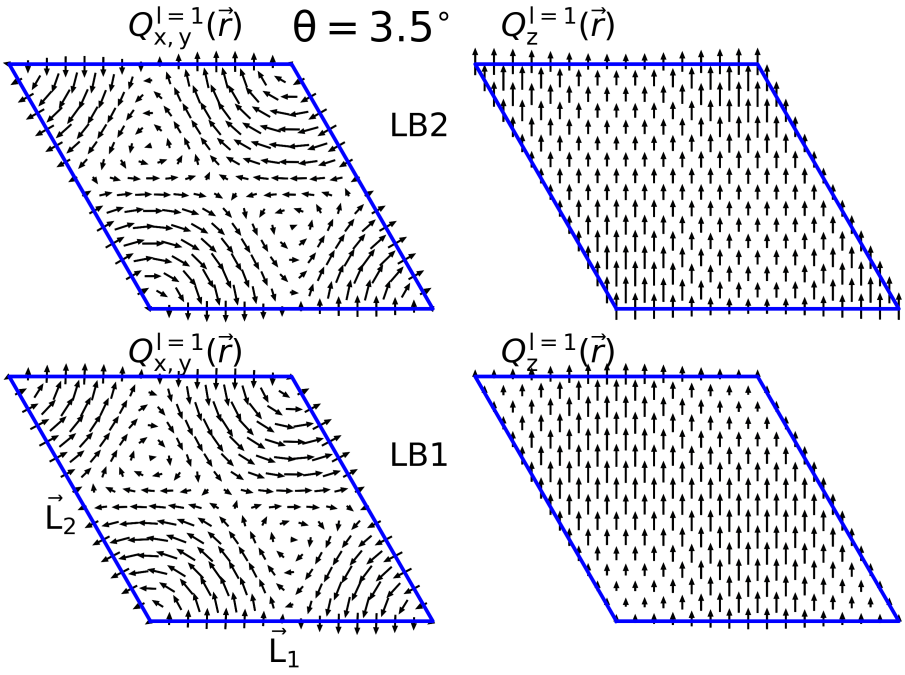

FIG. S14. Illustration of the eigenmodes $\mathbf{Q}(\mathbf{r})$ of the LB_1 (bottom row) and LB_2 (top row) modes at a twist angle of 3.5°. For simplicity only the mode components of the first layer ($l = 1$) are illustrated, the displacements of the second layer ($l = 2$) are given by $\mathbf{Q}^{l=1}(\mathbf{r}) = -\mathbf{Q}^{l=2}(\mathbf{r})$. Neighboring atoms in the same layer move in sync with each other. The left column shows the displacements in the xy-plane, the right column out-of-plane displacements (z). Displacements are enhanced for better illustration, $\mathbf{L}_{1/2}$ are the quasi supercell lattice vectors.

XII. DETAILS ON THE AB-INITIO CALCULATIONS

We have performed two types of ab-initio calculations. (A) A DFPT super cell calculation of single layer MoS_2 to evaluate the $\mathbf{q}$-dependent parts of the moiré dynamical matrix as defined in (Eq. S13) and (B) DFPT primitive

cell calculations of bilayer MoS_2 to sample the configuration space and evaluate the **q**-independent parts of $\bar{D}_{\mathrm{m}}$. In the following we will discuss the computational details of each type.

A. Details on the single-layer DFPT calculation

We used VASP[12, 13] in the local-density approximation (LDA), together with a 3×3×1 k-point sampling and a cutoff of 400 eV, in a 6×6×1 unit cell containing 108 atoms, with a lattice constant of 3.125 Å and a z-direction periodicity of 35 Å suppressing any coupling between the periodic images. The forces between atoms where calculated using PHONOPY[14] and VASP DFPT functionality. To account for an in total force free system, translational and rotational sum rules where enforced. To enforce the rotational sum rules we followed the implementation used in the Hiphive code[15]. The resulting single layer phonon dispersion relation is illustrated in Fig. S13a. The calculated phonon frequencies are in good agreement with existing literature[11].

B. Details on the bilayer DFPT

Components of the moiré dynamical matrix that couple the two layers are all evaluated at the **Γ**-point, as can be see from Eq. S13. We employ this **Γ**-point-only description, as it is sufficient to calculate the primitive cell bilayer system for various stacking configurations. We sample the configuration space on a 10×10 grid. For each configuration only the xy directions of the two Mo atoms are kept fixed and the system is otherwise allowed to minimize the Hellman-Feynman forces. Although fixing more than one atom results for most pristine stacking configurations in a slightly unstable structure, we expect the harmonic approximation to still be valid, since the anharmonic components stemming from xy displacements of the Mo atoms are expected to be very small.

For the calculation of the primitive cell bilayer system we use a 17×17×1 k-point grid in the simple LDA approximation with a cutoff of 400 eV and unit cell of 35 Å height. Although LDA is a rather crude approximation to account for Van-der-Waals coupled systems, it captures the layer separation reasonably well [9]. Fig. S15 illustrates the 3 configuration dependent interlayer Raman modes at the **Γ**-point. While the LB mode varies only by a comparatively small margin (≈ 15.6 cm^{-1}) for various stackings, the S modes vary over a far wider energy range, and lift their degeneracy, when the stacking configuration is moved away from a high symmetry point. Most importantly the S modes are unstable for most configurations, naturally forcing the system into an AB(BA) stacking configuration.

C. Details on the Raman intensity calculations

Off-resonant Raman intensity calculations as a function of layer separation where calculated in an AB stacking configuration using a scheme by Porezag et.al ([10]) sampling the layer separation between 6 and 6.75 Å in steps of 0.05 Å. Although fixing the layer separation will not result in meaningful results for the out-off-plane LB mode we expect the calculations to yield a useful guidance for the relative intensities of the in-plane S modes.

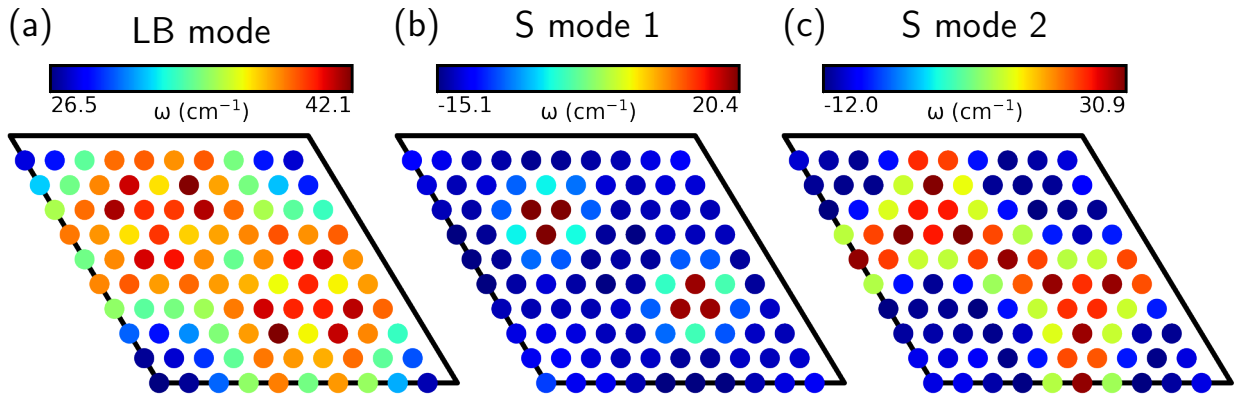

FIG. S15. The low energy phonon modes at the **Γ**-point, as sampled in configuration space. The positions of the dots correspond to the shift **d** between the two layers. (a) Illustrates the LB mode, (b) and (c) the two S modes, which are degenerate in AB(BA) (not exactly sampled) as well as AA stacking configurations.

[1] Nam, N. N. & Koshino, M. Lattice relaxation and energy band modulation in twisted bilayer graphene. *Phys. Rev. B* **96**, 075311 (2017).

[2] Carr, S. *et al.* Relaxation and domain formation in incommensurate two-dimensional heterostructures. *Phys. Rev. B* **98**, 224102 (2018).

[3] Koshino, M. & Son, Y.-W. Moiré phonons in twisted bilayer graphene. *Phys. Rev. B* **100**, 075416 (2019).

[4] Lee, J.-U. *et al.* Strain-shear coupling in bilayer MoS_2. *Nat. Commun.* **8**, 1370 (2017).

[5] Jung, J., Raoux, A., Qiao, Z. & MacDonald, A. H. Ab initio theory of moiré superlattice bands in layered two-dimensional materials. *Phys. Rev. B* **89**, 205414 (2014).

[6] Lin, M.-L. *et al.* Cross-dimensional electron-phonon coupling in van der waals heterostructures. *Nat. Commun.* **10**, 2419 (2019).

[7] Zhang, X. *et al.* Raman spectroscopy of shear and layer breathing modes in multilayer MoS_2. *Phys. Rev. B* **87**, 115413 (2013).

[8] Lin, M.-L. *et al.* Moiré phonons in twisted bilayer MoS_2. *ACS Nano* **12**, 8770–8780 (2018).

[9] Huang, S. *et al.* Low-frequency interlayer raman modes to probe interface of twisted bilayer MoS_2. *Nano Lett.* **16**, 1435–1444 (2016).

[10] Porezag, D. & Pederson, M. R. Infrared intensities and raman scattering activities within density-functional theory. *Phys. Rev. B* **54**, 7830–7836 (1996).

[11] Molina-Sánchez, A. & Wirtz, L. Phonons in single-layer and few-layer MoS_2 and WS_2. *Phys. Rev. B* **84**, 155413 (2011).

[12] Kresse, G. & Hafner, J. Ab initio molecular dynamics for liquid metals. *Phys. Rev. B* **47**, 558–561 (1993).

[13] Kresse, G. & Hafner, J. Ab initio molecular-dynamics simulation of the liquid-metal-amorphous-semiconductor transition in germanium. *Phys. Rev. B* **49**, 251–271 (1994).

[14] Togo, A. & Tanaka, I. First principles phonon calculations in materials science. *Scripta Mater.* **108**, 1–5 (2015).

[15] Eriksson, F., Fransson, E. & Erhart, P. The hiphive package for the extraction of high-order force constants by machine learning. *Adv. Theory Simul.* **2**, 1800184 (2019).